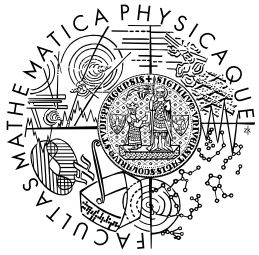

FACULTY
OF MATHEMATICS
AND PHYSICS
Charles University

BACHELOR THESIS

Maroš Bratko

Diagnostics of relativistic electron beams from laser accelerators

Department of Chemical Physics and Optics

Supervisor of the bachelor thesis: Ing. Jaroslav Nejdl, Ph.D.
Study programme: Physics
Study branch: General Physics

Prague 2021

I declare that I carried out this bachelor thesis independently, and only with the cited sources, literature and other professional sources. It has not been used to obtain another or the same degree.

I understand that my work relates to the rights and obligations under the Act No. 121/2000 Sb., the Copyright Act, as amended, in particular the fact that the Charles University has the right to conclude a license agreement on the use of this work as a school work pursuant to Section 60 subsection 1 of the Copyright Act.

In ..... date ....

Author's signature

Acknowledgement

I would like to express my immense gratitude to my supervisor Jaroslav Nejdl, and my two consultants Marcel Lamač and Uddhab Chaulagain, who guided me through the steps of writing this thesis. I would also like to thank Juan Carlos Hernandez Martin for help with technical matters, without whom the measurement of the magnetic field would not be feasible, and for his pleasant company. Additionally, I would like to thank my colleagues at ELI-Beamlines for providing a friendly and a pleasant work environment, in which all questions and ideas were welcomed. Lastly, I wish to thank my family and close friends for mental and emotional support throughout the time of writing this thesis.

This work was supported by the project ADONIS (CZ.02.1.01/0.0/0.0/16_019/0000789) from European Regional Development Fund and the project LM2015065 as part of targeted support of Large infrastructures of the Ministry of Education, Youth and Sports of the Czech Republic.

Title: Diagnostics of relativistic electron beams from laser accelerators

Author: Maroš Bratko

Department: Department of Chemical Physics and Optics

Supervisor: Ing. Jaroslav Nejdl, Ph.D., ELI Beamlines, Institute of Physics of the Czech Academy of Sciences

Consultant: Mgr. Marcel Lamač, ELI Beamlines, Institute of Physics of the Czech Academy of Sciences and Faculty of Mathematics and Physics, Charles University

Consultant: Dr. Uddhab Chaulagain, ELI Beamlines, Institute of Physics of the Czech Academy of Sciences

Abstract: Since the rise of high-energy particle physics in the 20th century, demands for radio-frequency particle accelerators have been increasing, leading to facilities occupying tens of square kilometers, requiring massive infrastructure, and having a very high cost. A promising alternative is laser wakefield acceleration, commonly referred to as LWFA, which is based on the interaction of intense laser pulse with the plasma. This technology produces accelerating fields four orders of magnitude larger than radio-frequency particle accelerators, greatly reducing its size. To evaluate the quality, stability, and reliability of the LWFA, properties of electron bunches emerging from the accelerator have to be investigated. The most important properties of electron bunches include the bunch charge, i.e. number of electrons in the bunch, energy distribution, divergence, bunch size, beam emittance, and pointing stability. This thesis is focused on the tools and detectors necessary for measuring these properties.

Keywords: laser plasma relativistic electron beams coherent transition radiation dipole magnet

Contents

Introduction **2**

1 Laser-driven Wakefield Accelerator **7**
1.1 Ponderomotive Force . . . 7
1.2 Plasma Generation . . . 8
1.3 Plasma Structures . . . 9
1.4 Waves in Plasma . . . 10
1.4.1 Nonlinear Plasma Waves . . . 12
1.5 Electron Injection . . . 15
1.6 Dephasing Length and Pump Depletion . . . 16

2 Transition Radiation **17**
2.1 Transition Radiation From a Single Electron . . . 17
2.1.1 Non-Ideal Case . . . 18
2.2 Electron Bunch Transition Radiation . . . 20

3 Relativistic electron beam diagnostics **22**
3.1 Integrating Current Transformer . . . 22
3.2 Magnetic Spectrometer . . . 23
3.2.1 Electron pointing . . . 24
3.2.2 Magnetic Spectrometer App . . . 26
3.3 Transition Radiation Detector . . . 29

4 Experimental Setup **32**
4.1 Integrating Current Transformer . . . 33
4.2 Magnetic Spectrometer . . . 34
4.2.1 Scintillator screen . . . 37
4.3 Transition Radiation Detector . . . 39

Conclusion **41**

Bibliography **42**

List of Figures **47**

A Appendix **49**
A.1 Ponderomotive force . . . 49
A.2 MidPoint method in Magnetic Spectrometer App . . . 50

Introduction

At the beginning of the 20th century, after the discovery of the electron by J. J. Thomson in 1897 [1], there was no scientific consensus on the structure of the atom. Following *Geiger–Marsden experiment* with α particles, also called *the Rutherford gold foil experiment*, Ernest Rutherford published his theory of atomic structure [2].
A few years later, in 1919, Ernest Rutherford observed "An Anomalous Effect in Nitrogen" [3], where unknown particles with positive charge and energy similar to hydrogen atoms emerged from the interaction of α particles with nitrogen in the air. We know currently, that the said particle was the proton, as portrayed on the post stamp from New Zealand shown in Figure 1 below. This was the very first case of artificial transformation from one element to another.

Figure 1: New Zealand post stamp portraying Ernest Rutherford. Reproduced from https://www.sciencedirect.com

Both aforementioned experiments utilized α particles emitted by naturally occurring radioactive elements (commonly used was Radium-226 and its daughter elements).
Rutherford believed, that he needed a more powerful stream of particles than those naturally emitted, i.e. with energies of the order of MeVs, to continue his research on the atomic nucleus, which was far beyond the technical capabilities at a time. When addressing the Royal Society in 1927 [4], Ernest Rutherford said: "*It has long been my ambition to have available for study a copious supply of atoms and electrons which have an individual energy far transcending that of the α and β-particles from radioactive bodies. I am hopeful that I may yet have my wish fulfilled, but it is obvious that many experimental difficulties will have to be surmounted before this can be realised, even on a laboratory scale.*"

However, in 1928, George Gamow [5][6] and Ronald Gurney [7] both independently predicted quantum tunneling, which implied lower energies required for Rutherford's research. Achieving these energies was technologically feasible, so Rutherford immediately assigned John Cockcroft and Ernest Walton to build a particle accelerator capable of energies of the order of hundreds of keV. Up to February 1932, they were able to produce protons with energies up to 700 keV using their first Cockcroft-Walton accelerator shown in Figure 2 below.

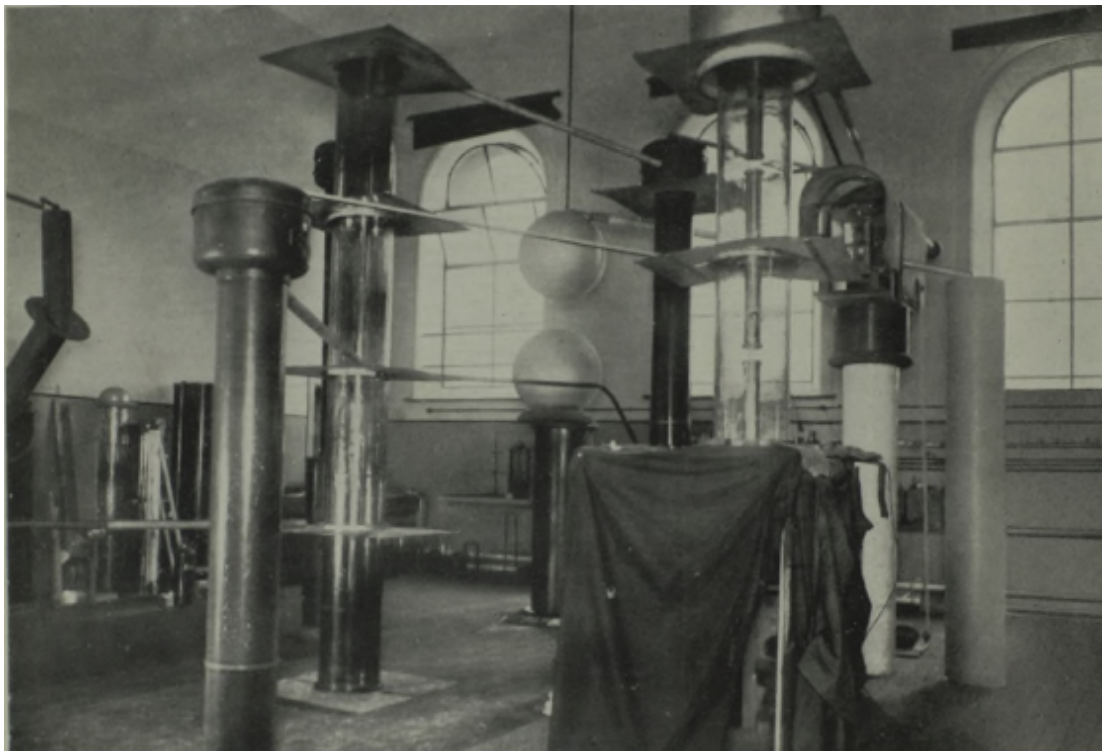

Figure 2: First Cockcroft-Walton Accelerator. Retrieved from [8]

A few months later, they successfully split the lithium atom [9]. This was the first splitting of the atom by artificially accelerated particles, for which both have been awarded the Nobel Prize in 1951.

Meanwhile, in 1931, Robert Jemison Van de Graaff was working on an electrostatic generator utilizing a moving belt for charge accumulation on a hollow metal sphere standing on the top of an insulated support cylinder. His prototype was able to reach a potential of 1.5 MVs [10] and was named after him. The generator possesses many advantages, as R.J. Van de Graaff himself stated in [10]: "The machine is simple, inexpensive, and portable. An ordinary lamp socket furnishes the only power needed."

Two years later, in 1933, the large Van de Graaff generator was under construction at Round Hill [11]. Its support cylinders were over 7 meters high and almost 2 meters wide, the spheres of aluminium were over 4.5 meters in diameter, and the whole generator occupied the airship dock on the estate of Colonel E. H. R. Green. The generator was expected to develop about 10,000,000 Volts. A schematic view of the large generator is shown in figure 3.

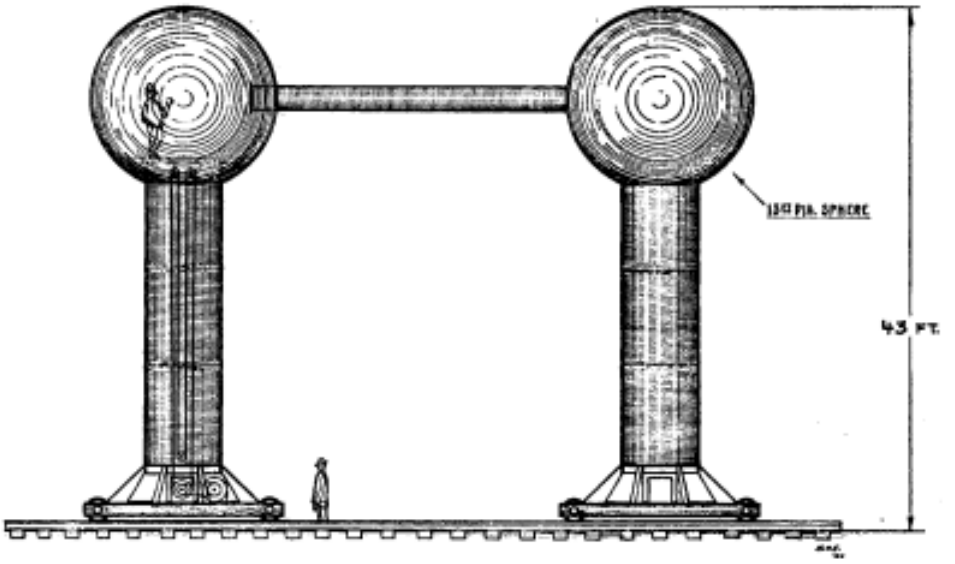

Figure 3: Schematic view of the large generator. Retrieved from [11]

Despite first successes, all aforementioned accelerators had a major flaw. The energy output of individual particles was limited by the maximum voltage created by the accelerator. The solution to this problem has already been proposed by Ising in 1924 [12]. The idea was to accelerate the particles with the same voltage repeatedly using the alternating fields.

In 1928, Ising suggested using a linear series of tubes with an alternating polarity connected to a radio-frequency generator, which was built on a small scale by Rolf Widerøe in 1928 [13]. This idea of a linear accelerator, known as *linac*, was replaced by a simpler idea proposed by Ernest Lawrence in 1932, the cyclotron [14]. A diagram of a cyclotron is shown in figure 4.

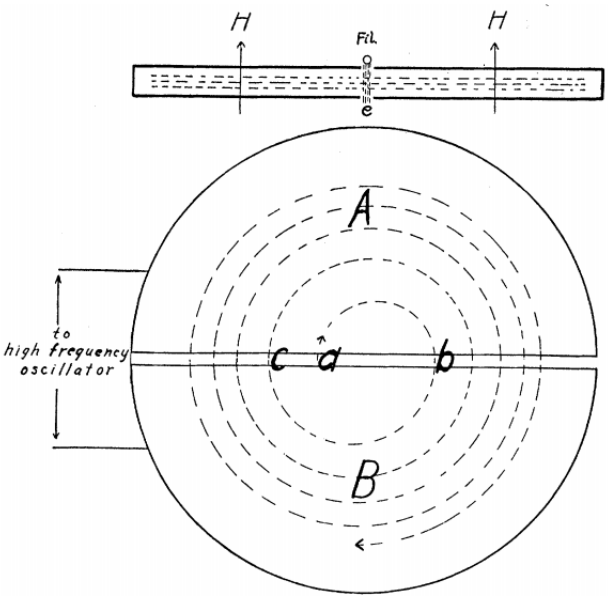

Figure 4: The diagram of a cyclotron. Retrieved from [14]

Two hollow semi-circular electrodes A and B with a gap between them are

placed between the poles of a magnet, which creates a magnetic field perpendicular to the plane of the electrodes. Both electrodes are connected to a radio-frequency generator with opposite polarity concerning each other. When there is a charged particle in the accelerator, it travels along the circular path, which is indicated by the arc $a - b$. At point b, the particle gets accelerated by the electric field created between electrodes and again travels along the circular path $b - c$. By adjusting the frequency, by the time it takes the particle to travel from point b to point c, the electric field is reversed and the particle is again accelerated. The time it takes the particle to complete one semi-circular path is independent of the velocity and radius of the particle, thus the frequency does not need to be changed during the process. Lawrence was able to obtain 1.22 MeV protons using this setup [14].

In 1944, Vladimir Veksler highlighted the sensitivity of the cyclotron to relativistic effects [15] and suggested a new method of accelerating relativistic particles. He solved this problem by inventing *synchrotron* utilizing *phase stability*. In a synchrotron, the guiding field increases with particles energy, thus both are *synchronized*, to keep the stationary orbit. The beam acceleration, bending, and focusing can be separated into different parts, which enables synchrotrons to be built on a large scale. Currently, the largest synchrotron-type accelerator is *Large Hadron Collider* (LHC) near Geneva with a 27-kilometre circumference [16] (shown on the figure 5 below). LHC holds the current world record for highest particle energy 6.5 TeV.

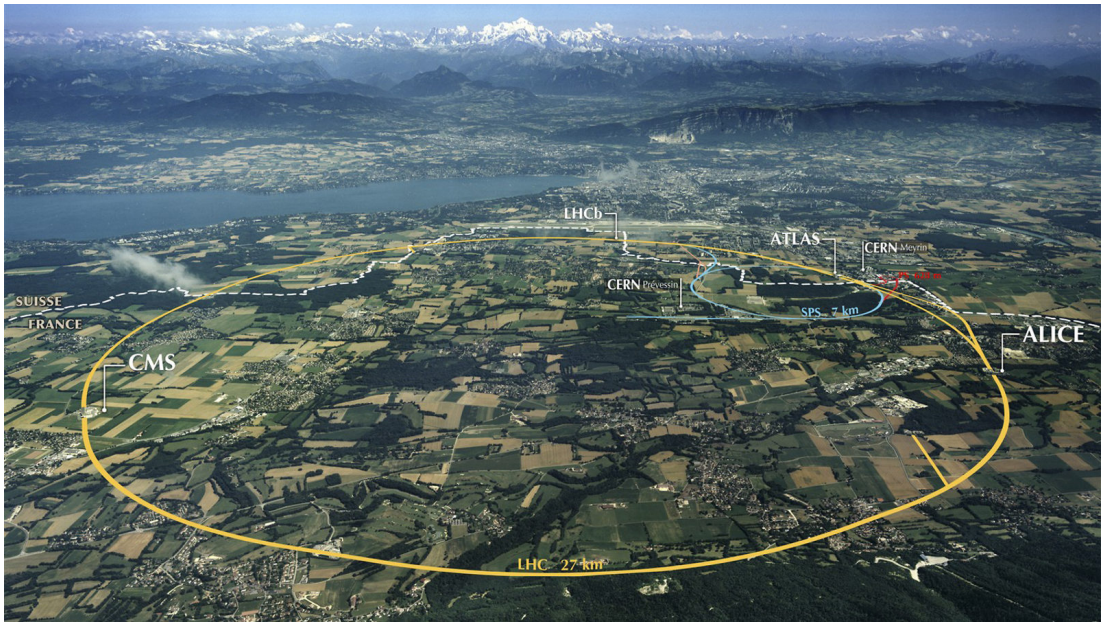

Figure 5: The scale of Large Hadron Collider. Reproduced from *Symmetry Magazine*

Over the years, there have been many other different types of accelerators utilizing different mechanisms. For example, the *betatron* accelerator with its concept suggested back in 1922 by Rolf Widerøe [17], where the circular particle beam acts as a secondary coil in a transformer. In 1950, Donald William Kerst was able to produce energies up to 315 MeV [18] using the betatron accelerator.

High-energy particles enable us to look into the nucleus of the atom and study the fundamental elements of matter. As shown on the previous page in the case of LHC, the size of the accelerator increases dramatically with the desired energy of particles. This disadvantage calls for more compact and cheaper alternatives. One concept, which is the focus of this thesis, is *Laser-driven Wakefield Accelerator*, usually reffered to as LWFA, proposed by Toshiki Tajima and John Myrick Dawson in 1979 [19]. Using petawatt laser technology, electrons with energy almost 8 GeV were produced over the distance of few centimeters [20].

In this thesis, I will present summary of available literature necessary for understanding how LWFA and diagnostics methods developed for it work. In **Chapter 1** I will describe the interaction between laser and charged particles, and how the underlying mechanism of LWFA and its characteristic properties emerge from it. In **Chapter 2** I will show the theoretical description of Transition Radiation, its basic properties of its spectrum, its limitations outside of idealistic conditions, and show its potential for measuring the spatial distribution of electron bunch. In **Chapter 3** I will illustrate and explain mechanisms behind 3 available diagnostics for measuring properties of electron bunches from LWFA, and show tools developed for them. In **Chapter 4**, I will illustrate the experimental setup for LWFA experiment at Dolní Břežany, Czech Republic, its parameters, and devices used in the experiment. Numerical calibration of the magnetic spectrometer will be performed, as well as outline of the future Transition Radiation Detector will be shown and discussed.

1. Laser-driven Wakefield Accelerator

The main disadvantage of radio-frequency particle accelerators is their limit for maximum accelerating fields $\sim$ 50 MV/m due to the breakdown of metals, and also the melting point of copper [21]. Therefore, one has to build large-scale facilities with expensive infrastructure to obtain high-energy particles.

Laser-driven Wakefield Accelerators (LWFA) based on the interaction of the laser pulse with the plasma, can produce accelerating fields over $\sim$ 100 GV/m [22], which are up to four orders of magnitude larger than radio-frequency particle accelerators.

1.1 Ponderomotive Force

To understand the principle behind the LWFA, from which the majority of properties of LWFA emerge, we have to study the interaction of an oscillating electromagnetic field of a laser pulse and a charged particle. The following explanation was inspired by [23].

Let us consider a laser pulse propagating in the positive direction along the z-axis polarized in the $x-z$ plane. We can characterize this pulse coordinates by a vector potential $\boldsymbol{A} = A(z,t)\boldsymbol{e}_\perp$ is the unit vector perpendicular to the propagation direction of the laser pulse. This laser pulse affects the motion of a particle with a charge q and a mass m via the Lorentz force. We can express the Lorentz force through the said vector potential as follows

$$\frac{\mathrm{d}\boldsymbol{p}}{\mathrm{d}t} = q\left[-\frac{\partial \boldsymbol{A}}{\partial t} + \frac{\boldsymbol{p}}{m} \times (\nabla \times \boldsymbol{A})\right], \tag{1.1}$$

where $\boldsymbol{p}$ denotes the momentum of the particle and $\nabla = (\partial/\partial x\ , \partial/\partial y\ , \partial/\partial z)$ is the differential operator.

Since we assumed a non-relativistic case, the contribution of a magnetic field (second term in 1.1) is much smaller than the contribution of an electric field (first term in 1.1), thus we can separate the momentum of the particle into two parts $\boldsymbol{p} = \boldsymbol{p_1} + \boldsymbol{p_2}$, where $\boldsymbol{p_2} \ll \boldsymbol{p_1}$. By plugging this sum into the (1.1) and comparing the magnitudes on both sides, we can identify the first part of the particle's momentum as $\boldsymbol{p_1} = -q\boldsymbol{A}$. We can see, that the major part of particle's motion will consist of oscillations in the laser's plane of polarization, i.e. $x-y$ plane.

What we are now left with in the (1.1) is the equation for the second part of particle's momentum. By using the assumption $\boldsymbol{p_2} \ll \boldsymbol{p_1}$ and the result $\boldsymbol{p_1} = -q\boldsymbol{A}$, we can approximate this momentum as

$$\frac{\mathrm{d}\boldsymbol{p_2}}{\mathrm{d}t} \approx -\frac{q^2}{m}\boldsymbol{A} \times (\nabla \times \boldsymbol{A}) = -\frac{q^2}{2m}\nabla|\boldsymbol{A}|^2 = -\frac{q^2}{2m\omega^2}\nabla|\boldsymbol{E}|^2\,, \tag{1.2}$$

where we used the identity $\boldsymbol{A} \times (\nabla \times \boldsymbol{A}) = \frac{1}{2}\nabla|\boldsymbol{A}|^2 - (\boldsymbol{A}\cdot\nabla)\boldsymbol{A}$ in the second equality ($(\boldsymbol{A}\cdot\nabla)\boldsymbol{A}$ is identically zero, check appendix A.1).

We can see, that while the particle is oscillating in the $x - y$ plane, it is also pushed in the direction of a decreasing electric intensity, which in our case happens only in the z-direction, regardless of the sign of their charge. In other words, the laser pulse *"pushes away"* both positive and negative particles from the regions of high electric intensity. This force, expressed in this non-relativistic case via the equation (1.2), is called the *Ponderomotive Force*.

1.2 Plasma Generation

In this thesis, we will consider plasma as a quasi-neutral medium consisting of positively charged ions and negatively charged electrons. In the laboratory, we can create a plasma by focusing an intense laser onto a gas target.

In 1965, L. V. Keldysh developed a theory of "*Ionization in the field of a strong electromagnetic wave*" [24], which describes different regimes of gas ionization induced by a laser. Keldysh has shown, that photoionization is dominated by two pathways - *multiphoton ionization* and *electron tunneling*. The transition from one pathway to the other is determined by a single parameter, called the *Keldysh gamma parameter*, given by the expression[25]

$$\Gamma = \frac{\omega\sqrt{2m_e I_p}}{eE_0}\,, \tag{1.4}$$

where ω is the frequency of the laser, m_e is the rest mass of the electron, I_p is the ionization potential, i.e. the energy required to separate the electron from an atom, e is the elementary charge, and E_0 is the amplitude of the driver field (laser in the case of LWFA).

When $\Gamma \gg 1$, the photo-ionization is dominated by multiphoton ionization and the photo-ionization rate depends strongly on the frequency of the laser. When $\Gamma \ll 1$, the potential of the nucleus is strongly modified by the electric field (as shown on figure 1.1 below) and the photo-ionization occurs mostly through the electron tunneling. At this point, the photo-ionization rate is frequency-independent.

Using the Keldysh gamma parameter, we can estimate the intensity of a laser corresponding to the boundary ($\Gamma = 1$) between two photo-ionization regimes. We can relate the amplitude E_0 of the driver field to the intensity of the laser I by the relation $I = E_0^2/2Z_0$, where Z_0 is the impedance of the vacuum. By plugging the $\omega = 2\pi c/\lambda$ into the equation (1.4), where c is the speed of light and λ is the wavelength of the laser, we can get the expression for the estimated laser intensity

$$I = \frac{4\pi^2 c^2 m_e I_p}{\lambda^2 e^2 Z_0 \Gamma^2}\,. \tag{1.5}$$

In practical units we get

$$\boxed{I(\mathrm{W/cm^2}) \simeq 5 \cdot 10^{14} \frac{I_p(\mathrm{eV})}{[\lambda(\mathrm{nm})\Gamma]^2}} \tag{1.6}$$

By plugging in $\Gamma = 1$ for helium ($I_p = 24.6$ eV [26]), the intensity of the 800 nm laser corresponding to the boundary $\Gamma = 1$ is approximately $2 \cdot 10^{10}$ W/cm^2.

Experimentally, lasers with intensities approximately $\sim 10^{15}$ W/cm^2 are capable of ionizing the helium [27].

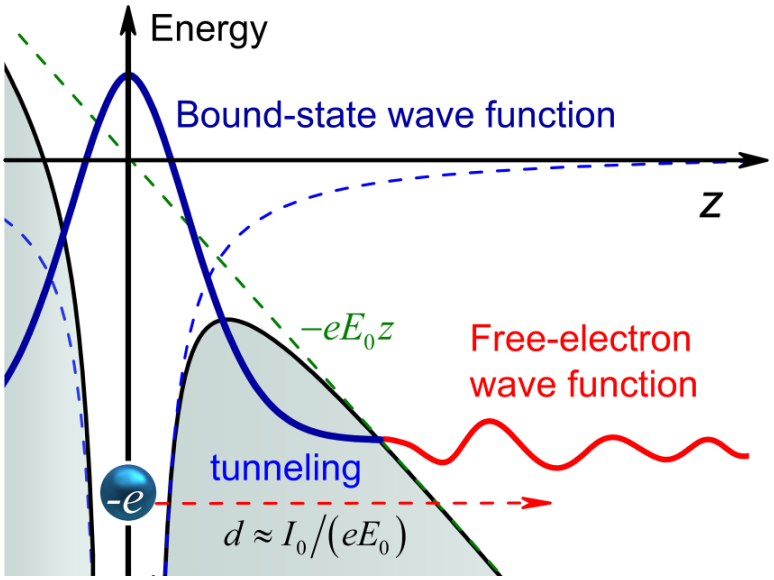

Figure 1.1: Tunneling of the electron through the potential of the atomic nucleus. Reproduced from [25]

1.3 Plasma Structures

As a consequence of the relatively high mass of positively charged ions - atomic nuclei (with respect to electrons) and the inverse dependence of ponderomotive force on their mass (equation 1.2), their space displacement can be neglected and we can treat them as a non-moving positively charged background. Therefore we can take into consideration only the displacement of free electrons.

As a laser pulse propagates through the plasma along the z-axis, it causes the negatively charged electrons to move towards the area of a weaker field strength via ponderomotive force described in the previous chapter. This leaves a positively charged and nearly spherical cavity behind the laser pulse called *"wake"*. As a result, electrons around the wake will accelerate into this cavity via the Coulombic interaction, pass over the equilibrium position, and begin to oscillate with the following frequency called the *plasma frequency* [28]

$$\boxed{\omega_p = \sqrt{\frac{e^2 n_e}{\varepsilon_0 m_e}}} \tag{1.7}$$

Here, ε_0 denotes the permittivity of the free space and n_e denotes the plasma electron density.

It is important to note, that the phase velocity of the resulting plasma structure is determined by the driver [23], a group velocity of the laser pulse in our case.

A change in plasma density also creates enormous accelerating (longitudinal) fields. To estimate the magnitude of such fields, we can use Gauss's law in the differential form (the following procedure was inspired by [29]).

Let $\overline{n}_e$ be the electron density of the unperturbed plasma. Let's consider the following sinusoidal change in the electron density

$$\delta n_e(z,t) = \delta n_{e,0} \cos(k_p z - \omega_p t)\,, \tag{1.8}$$

where $\delta n_e(z,t) = n_e - \overline{n}_e$ is the electron density perturbation and $k_p = \omega_p/c$. We have assumed, that the density perturbation propagates nearly at the speed of light $v_p \approx c$.
By plugging the equation (1.8) into Gauss's law we get

$$\frac{\partial E_z}{\partial z} = \frac{\delta n_{e,0} e}{\varepsilon_0} \cos(k_p z - \omega_p t) \implies E_z = \frac{\delta n_{e,0} e c}{\omega_p \varepsilon_0} \sin(k_p z - \omega t) \tag{1.9}$$

Since the maximum density perturbation can be of order $\delta n_{e,0} \approx \overline{n}_e$, we get the maximum accelerating field to be approximately

$$E_{z,0} \approx \sqrt{\frac{m_e \overline{n}_e}{\varepsilon_0}} c \implies \boxed{E_{z,0}(\mathrm{V/m}) \approx 96\sqrt{\overline{n}_e(\mathrm{cm}^{-3})}} \tag{1.10}$$

Since practical electron plasma densities range $10^{17} < \overline{n}_e < 10^{19}$ cm^{-3} [29], then achievable accelerating fields are of order $E_{z,0} \approx 100$GV/m, as discussed previously.

To describe the conditions under which these phenomenons occur, it is good practice to define a dimensionless normalized vector potential $\boldsymbol{a} = e\boldsymbol{A}/m_e c$. When $\boldsymbol{a}$ approaches unity, the plasma becomes non-linear and relativistic.

1.4 Waves in Plasma

Since we assumed the plasma to be quasi-neutral medium consisting of positive ions and negative electrons, variety of waves can propagate throughout the plasma. We can investigate the electromagnetic modes without the presence of a stationary magnetic field using the Maxwell's equations in vacuum in the differential form [30]

$$\nabla \cdot \boldsymbol{E}(\boldsymbol{r},t) = \frac{\rho(\boldsymbol{r},t)}{\varepsilon_0}\,, \tag{1.11}$$

$$\nabla \cdot \boldsymbol{B}(\boldsymbol{r},t) = 0\,, \tag{1.12}$$

$$\nabla \times \boldsymbol{E}(\boldsymbol{r},\boldsymbol{t}) = -\frac{\partial \boldsymbol{B}(\boldsymbol{r},t)}{\partial t}\,, \tag{1.13}$$

$$\nabla \times \boldsymbol{B}(\boldsymbol{r},t) = \mu_0 \boldsymbol{j}(\boldsymbol{r},t) + \mu_0 \varepsilon_0 \frac{\partial \boldsymbol{E}(\boldsymbol{r},t)}{\partial t}\,, \tag{1.14}$$

where μ_0 is the permeability of vacuum, $\rho(\boldsymbol{r},t)$ is the electric charge density and $\boldsymbol{j}(\boldsymbol{r},t)$ is the electric current density.

By taking the curl of the equation (1.13) and using the (1.14) we get the following equation

$$\nabla \times \nabla \times \boldsymbol{E}(\boldsymbol{r},t) = -\frac{1}{c^2}\left(\frac{1}{\varepsilon_0}\frac{\partial \boldsymbol{j}(\boldsymbol{r},t)}{\partial t} + \frac{\partial^2 \boldsymbol{E}(\boldsymbol{r},t)}{\partial t^2}\right). \tag{1.15}$$

Considering the freely moving electrons in plasma as we discussed previously, the electric force acting upon them is $\boldsymbol{F}(\boldsymbol{r},t) = -e\boldsymbol{E}(\boldsymbol{r},t)$. Since the mass of the electrons does not change, their acceleration becomes $\partial \boldsymbol{v}(\boldsymbol{r},t)/\partial t = -e\boldsymbol{E}(\boldsymbol{r},t)/m_e$. As a result, these electrons create an electric current, which can be expressed as $\boldsymbol{j}(\boldsymbol{r},t) = -en_e\boldsymbol{v}(\boldsymbol{r},t)$.

By combining these two expressions, the equation (1.15) takes the following form

$$\nabla \times \nabla \times \boldsymbol{E}(\boldsymbol{r},t) = -\frac{1}{c^2}\left(\frac{n_e e^2}{\varepsilon_0 m_e}\boldsymbol{E}(\boldsymbol{r},t) + \frac{\partial^2 \boldsymbol{E}(\boldsymbol{r},t)}{\partial t^2}\right). \tag{1.16}$$

Applying the Fourier-transform with respect to time and three spatial dimensions $\boldsymbol{E}(\boldsymbol{r},t) = \int_{R\times R^3} \boldsymbol{E}(\boldsymbol{k},\omega)e^{i(\boldsymbol{k}\cdot\boldsymbol{r}-\omega t)}\mathrm{d}\omega\mathrm{d}^3k$ we get the condition for $\boldsymbol{E}(\boldsymbol{k},\omega)$ as follows

$$\boxed{\boldsymbol{k}\times\boldsymbol{k}\times\boldsymbol{E}(\boldsymbol{k},\omega) = \frac{1}{c^2}\left(\omega^2 - \frac{n_e e^2}{\varepsilon_0 m_e}\right)\boldsymbol{E}(\boldsymbol{k},\omega)} \tag{1.17}$$

We can immediately see, that the second term in brackets on the right side of the equation (1.17) corresponds to the plasma frequency. When $\boldsymbol{k} \parallel \boldsymbol{E}$, the left side is identically zero, and the frequency of the wave is equal to the plasma frequency.

From the equation (1.17) we can also determine what kind of electromagnetic waves propagate through the plasma. By plugging $\boldsymbol{k} \perp \boldsymbol{E}$, which corresponds to electromagnetic waves, into the equation (1.17), we get the following dispersion relation for electromagnetic waves in plasma

$$\boxed{\omega^2 = \omega_p^2 + k^2c^2} \tag{1.18}$$

We can immediately see from the equation (1.18), that only the electromagnetic modes with $\omega > \omega_p$ can propagate through the plasma (k is real). If $\omega < \omega_p$, then the k is imaginary and the electromagnetic wave does not propagate in the plasma.

From the equation (1.18) we can determine the velocities of the electromagnetic waves in plasma. Using the definition of the phase velocity we get the following result

$$v^{\text{phase}} = \frac{\omega}{k} = \frac{c}{\sqrt{1-\omega_p^2/\omega^2}}. \tag{1.19}$$

Using the definition of the group velocity we get

$$v^{\text{group}} = \frac{\mathrm{d}\omega}{\mathrm{d}k} = c\sqrt{1-\omega_p^2/\omega^2}. \tag{1.20}$$

As discussed in chapter 1.3, the phase velocity of the plasma structure is determined by the group velocity of the laser pulse. Thus we see, that the plasma structure ("wake") propagates through the plasma at speeds slower than the speed of light.

1.4.1 Nonlinear Plasma Waves

In the linear regime, where $E < E_{z,0}$ determined by the equation 1.10, the plasma wave oscillates sinusoidally [23], as we assumed in the section 1.3. However, when $E > E_{z,0}$, the plasma starts to behave non-linearly and oscillations diverge from sinusoidal oscillations.

To examine this situation in 1D, it is practical to work with plasma as fluid instead of a finite set of particles, since we are interested only in macroscopic quantities, such as an electron density n_e. We also assume a non-evolving drive laser pulse, i.e. the drive laser pulse only depends on the $\xi = z - v_p t$, where $v_p \simeq v^{\text{group}}$ is the phase velocity of the plasma wave approximately equal to the group velocity of the drive pulse [23]. Under these assumptions, the analytic solution for the relativistic plasma ($\gamma_p^2 \gg 1$) to the 1D Poisson's equation $\partial^2\phi_n/\partial\xi^2 = k_p^2\,(n_e/n_0 - 1)$ for normalized electric potential $\phi_n = e\phi/m_e c^2$, where n_e is the electron density and the n_0 is the equilibrium density, is [23]

$$\frac{\partial^2\phi_n}{\partial\xi^2} = \frac{k_p^2}{2}\left[\frac{1+a^2}{(1+\phi_n)^2} - 1\right], \tag{1.21}$$

where $k_p = \omega_p/v_p$ is the wave-number of the plasma wave and a is the normalized vector potential mentioned in the section 1.3.
The equation 1.21 is called the *relativistic non-linear one-dimension plasma wave equation*. The electron plasma density n_e normalized to the equilibrium density n_0 is then [23]

$$\frac{n_e}{n_0} = \frac{1 + a^2 + (1+\phi_n)^2}{2(1+\phi_n)^2}\,. \tag{1.22}$$

Numerical solutions to the equation (1.21) for different laser pulses are shown on the figure 1.2 below. We used a Gaussian pulse with length l_L (FWHM) described by $a(\xi) = a_0 \exp(-4\xi^2/l_L^2 \ln 2)$ (green area), where we chose the length of the laser pulse to be $l_L = 0.4\lambda_p$. Solutions were computed for pulses with the amplitude of normalized vector potential $a_0 = 0.1$, $a_0 = 1$ and $a_0 = 2$. Deviations of electron density from equilibrium normalized to equilibrium density is shown by the blue line (unity subtracted from the equation 1.22). Normalized accelerating electric fields E_n calculated as a negative first derivative of the normalized potential given by the equation (1.21) are also shown by the red line. ξ is given in the multiples of plasma wavelength $\lambda_p = 2\pi v_p/\omega_p$.

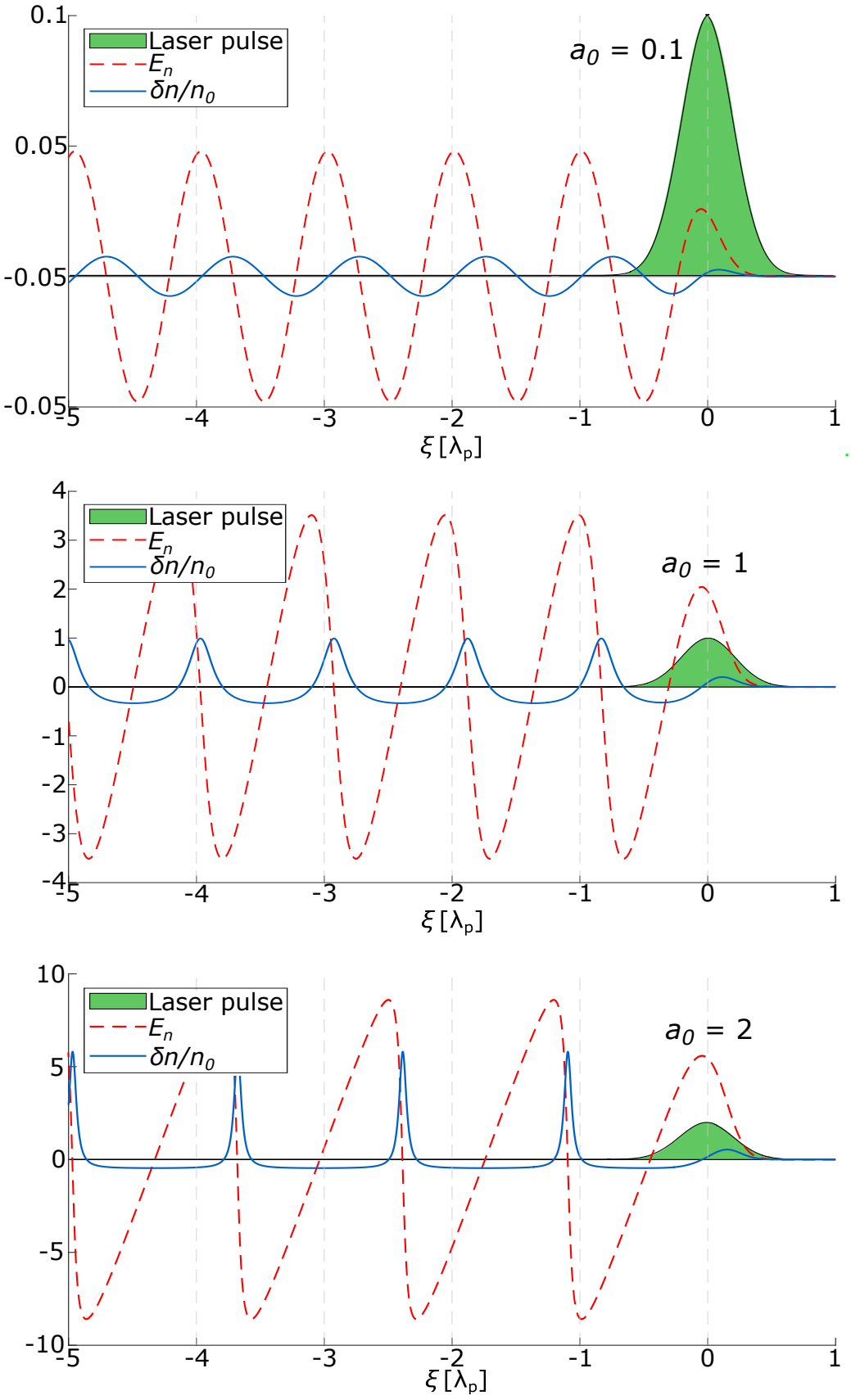

Figure 1.2: Numerical solutions to the equation (1.21) for right-propagating lasers. The green area depicts the laser pulse, the blue line are the density oscillations(equation 1.22), the red line shows the accelerating fields.

We can see, that in the linear case ($a_0 = 0.1$), oscillations of electron plasma density δn_e and normalized accelerating electric fields E_n are both sinusoidal. When we start to enter the non-linear regime ($a_0 = 1$), the oscillations of electron plasma density are of the order of the equilibrium density n_0, as we expected in section 1.3. In the relativistic non-linear regime ($a_0 = 2$), the density oscillations have sharp spikes separated roughly by a plasma wavelength λ_p and accelerating fields take on a saw-tooth-like form.

We can investigate the relationship between the length of the pulse and intensity of density oscillations by numerically solving the equation (1.21). We used same Gaussian pulse as in a previous case with $a_0 = 1$ and different lengths. For each pulse length we took the maximum of the density oscillations. The numerical results are shown on the Figure 1.3.

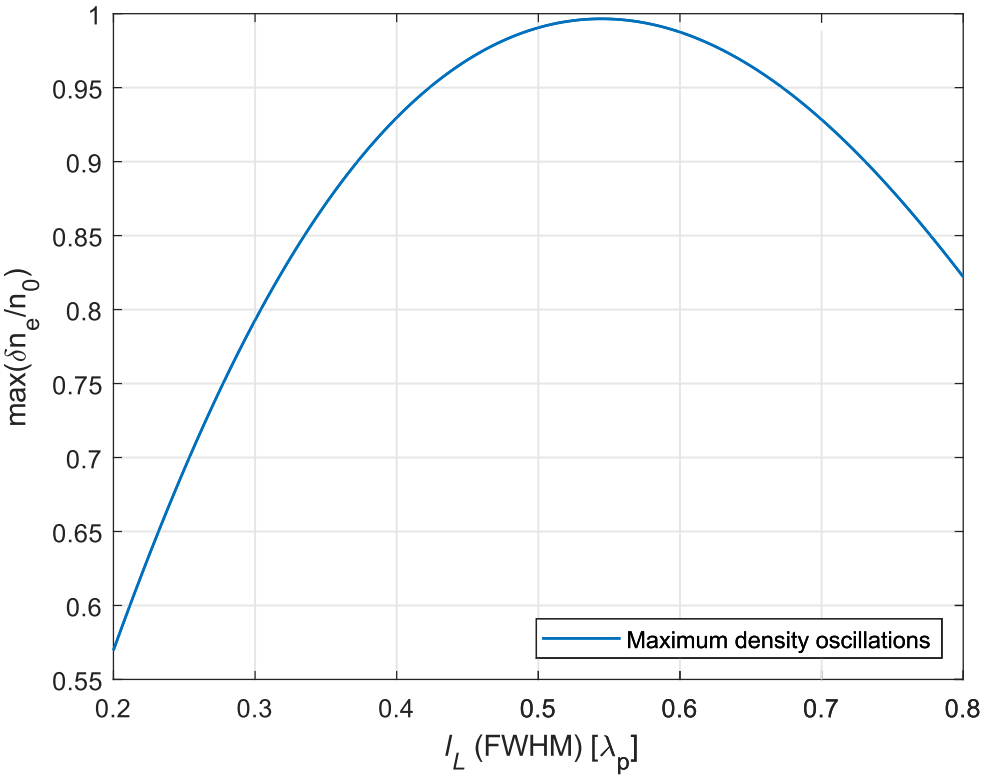

Figure 1.3: Calculated maximum density oscillations created by laser pulses with different lengths. In all cases, normalized vector potential amplitude was $a_0 = 1$.

We can see, that the magnitude of density oscillations is the greatest, when the length of the laser pulse is approximately half of the plasma wavelength, i.e.

$$\boxed{l_L \simeq \frac{\lambda_p}{2}} \tag{1.23}$$

This condition emerges from the resonance between the ponderomotive force and the electron oscillations [31].

1.5 Electron Injection

Once the accelerating plasma structure - *wake* - has been formed, electrons have to be *injected* into the plasma structure in order to be accelerated. This can happen through a variety of mechanisms.

Self-injection occurs when the laser pulse is strong enough to expel almost all the electrons, which then accumulate at the back of the cavity. Once the electron density passes certain threshold, the accelerating structure becomes unstable and electrons get trapped in the accelerating field. In other words, the self-injection occurs when the laser pulse is strong enough to break out the electrons from the plasma structure itself. The main advantage of this scheme comes from the fact, that it only requires sufficient laser intensity to occur. However, this method produces electron bunches with a large energy spread [32][29].

Colliding-pulse injection utilizes a second laser pulse colliding head-on with the main pulse. This produces a ponderomotive force with an amplitude proportional to the product of the amplitudes of both pulses. This method can induce injection below its self-injection threshold. Experimentally, electron beam of 10 pC with energy 200 MeV and energy spread $\Delta E^{(\mathrm{FWHM})}/E \approx 0.01$ has been reported [33].

Down-ramp injection relies on decreasing the electron plasma density along the path of the wake. It follows from the equation (1.20) and (1.7), that the phase velocity of the wake will decrease, which encourages injection [32]. One or more down-ramps with different density profiles can be used. Mono-energetic electron beams with energies between 15 and 25 MeV with 3.3 pC charge on average were reported [34] using this method.

Ionization injection uses additional admixtures with higher Z (proton number), such as nitrogen N_2 or oxygen O_2, mixed into the original gas, usually Helium He or hydrogen H_2 [35] [36]. The mechanism behind ionization injection emerges naturally from the equation (1.6). The leading edge of the laser pulse ionizes the electrons of lighter gas and the outer electrons of the heavier gas because they have smaller ionization potential I_p. Main part of the pulse then creates the accelerating structure and ionizes the inner electrons of the heavier gas. These electrons are then trapped by inner electric fields of the wake and get accelerated below the self-injection threshold. Electron beam of charge 10 pC, energy $E > 1$ GeV and energy spread $\Delta E^{(\mathrm{FWHM})} < 100$ MeV has been obtained experimentally using ionization injection [37].

1.6 Dephasing Length and Pump Depletion

In the accelerating cavity, the accelerated electrons are travelling at almost the speed of light, while the accelerating cavity propagates through the plasma at the group velocity of the laser pulse given by the equation (1.20). As a result, electrons move through the accelerating cavity at the speed $c - v^{\text{group}}$. From the Figure 7 we can see, that the accelerating electric fields are located only in the first half of the accelerating cavity, which is approximately half the plasma wavelength, i.e. $\sim \lambda_p/2$. As the electrons reach the center of the accelerating cavity, they are no longer accelerated. This limits the maximum energy gain of the beam.

The time it takes the electrons to reach the center of the accelerating cavity is approximately $\sim \lambda_p/[2(c - v^{\text{group}})]]$. The distance over which they are then accelerated, called the *dephasing length* L_d, is therefore $\sim c\lambda_p/[2(c - v^{\text{group}})]$. Using the equation (1.20) we get, that the dephasing length in the practical units is approximately [29]

$$L_d(cm) \approx \frac{3.7}{[\overline{n}_e(10^{18}\text{cm}^{-3})]^{3/2}[\lambda(\mu\text{m})]^2}\,, \tag{1.24}$$

where $\overline{n}_e$ is the equilibrium electron density and λ is the wavelength of the laser pulse. For $\overline{n}_e = 10^{18}$ cm^{-3} and $\lambda = 1\mu$m we get the dephasing length $L_d \approx 3.7$ cm, which limits the energy gain to approximately $\Delta W \approx eE_{z,0}L_d \approx 3.7$ GeV. We can also notice from the equation (1.20) and the equation (1.7), that we can compensate this effect by introducing density up-ramp ($\mathrm{d}\overline{n}_e/\mathrm{d}z > 0$), which will keep the accelerated bunch at the rear of the wake [29], since the plasma wavelength decreases with the increasing $\overline{n}_e$.

Another effect, which limits the effective length of the electron acceleration, is the depletion of the laser pulse, i.e. *pump depletion*.

It has been shown in 3D numerical simulations, that in the nonlinear ($a_0 > 1$) and short-pulse ($\omega_p\tau_L < 1$) regime, where the τ_L is the duration of the pulse, the effective acceleration distance due to the pump depletion is in the laboratory units given by [38]

$$L_{pd}(\text{cm}) \approx \frac{0.03\tau_L(\text{fs})}{\overline{n}_e(10^{18}\text{cm}^{-3})[\lambda(\mu\text{m})]}\,. \tag{1.25}$$

For $\tau_L = 100$ fs, $\overline{n}_e = 10^{18}$ cm^{-3} and $\lambda = 1\mu$m, we get $L_{pd} \approx 3$cm, which is similar to the dephasing length. There are currently no method to compensate pump depletion [29].

2. Transition Radiation

Transition radiation (TR) is emitted, when a uniformly moving charged particle passes through a boundary between two media with different dielectric constants, for example a vacuum and a metal. It was first theoretically described by Ginzburg and Frank in 1946 [39].

Variety of approaches have been used to describe the theoretical properties of the Transition Radiation. They all involve solving field equations for both media and connecting them via boundary/interface conditions. This can be either performed directly [40], or by considering the fact, that for the observer, the charge passing through the boundary annihilates with its virtual opposite charge [41], which can be interpreted as if both charges came to stop instantaneously. The accelerating charge then emits the electromagnetic radiation, as illustrated on the Figure 2.1.

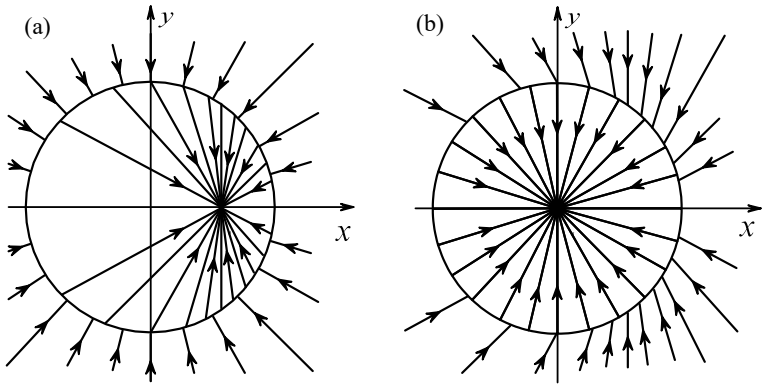

Figure 2.1: Electric field of charge (a) instantaneously starting, (b) instantaneously stopping. Reproduced from [41]

For the method of Transition Radiation derivation using the theory of generalised functions (distributions), we refer the kind reader to [42].

2.1 Transition Radiation From a Single Electron

Let's assume the electron passing the step-like boundary between the semi-infinite ideal conductor (with relative permittivity $|\epsilon_2| \to \infty$) and the vacuum (with relative permittivity $\epsilon_1 = 1$) perpendicularly to the boundary at the speed v. We also assume, that the distance between the source of the radiation and the observer is larger than the *formation length* $L_f \sim \lambda\gamma^2$ [40] (where λ is the wavelength of the emitted TR, and γ is the Lorentz factor of the electron), which means we are working in the *far-field* regime. *Formation length* is the distance, over which the Coulomb field and radiation field separate [43]. Then the energy radiated from a single electron into the solid angle $\mathrm{d}\Omega$ per unit frequency $\mathrm{d}\omega$ is given by [40]

$$\frac{\mathrm{d}^2 W_e}{\mathrm{d}\Omega \mathrm{d}\omega} = \frac{r_e m_e c}{\pi^2} \frac{\beta^2 \sin^2\theta}{(1-\beta^2\cos^2\theta)^2}\,, \tag{2.1}$$

where θ is the angle between the observation direction and the electron propagation, $\beta = v/c$ is the normalized electron velocity, r_e is the classical electron radius $r_e = e^2/(4\pi\epsilon_0 m_e c^2)$, m_e is the mass of the electron and c is the speed of light.

We can see that no energy is emitted forward, since the equation (2.1) vanishes on axis ($\theta = 0$). For highly relativistic electrons ($\gamma \gg 1$), the distribution given by the equation (2.1) peaks at $\theta \simeq 1/\gamma$, i.e. width of the radiating cone corresponds to the particle's energy. We can also see, that the distribution is axially symmetric.

Calculated far-field intensity profile of the $\approx$ 100 MeV electron ($\gamma = 200$) given by the equation (2.1) is shown on Figure 2.2.

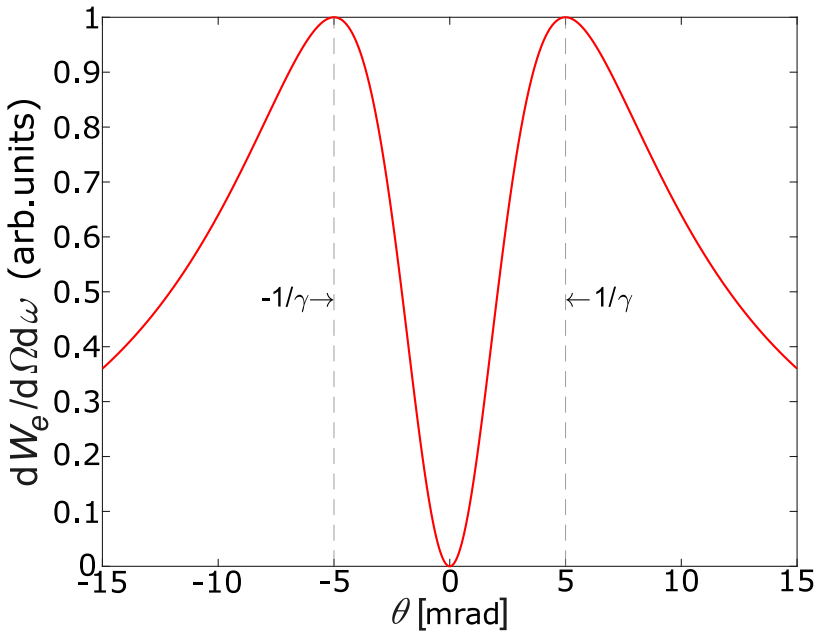

Figure 2.2: Far-field intensity profile of 100 MeV electron given by the equation (2.1)

It is important to note, that the axial symmetry holds only in the case of a single electron propagating *perpendicularly* to the boundary between conductor and vacuum. In case of electron passing the boundary obliquely, the symmetry breaks [29].

2.1.1 Non-Ideal Case

The equation (2.1) only holds for the perfect semi-infinite conductor, for which the magnitude of dielectric constant (relative permittivity) $|\epsilon|$ is infinite. We can therefore use the equation (2.1) only for materials with dielectric constant such that $|\epsilon| \gg 1$. However, in the case of an imperfect conductor (or any other material), the dielectric constant is a complex number not far from unity. When the particle with charge q crosses the boundary between two semi-infinite media with arbitrary dielectric constants ϵ_1 and ϵ_2 at a normalised speed β perpendicular

to the boundary, the power distribution $\mathrm{d}^2W/\mathrm{d}\Omega\mathrm{d}\omega$ takes the following form [44]

$$\frac{\mathrm{d}^2W}{\mathrm{d}\Omega\mathrm{d}\omega} = \frac{q^2\beta^2\sqrt{\epsilon_2}\sin^2\theta\cos^2\theta}{4\pi^3\epsilon_0 c(1-\beta^2\epsilon_2\cos^2\theta)^2} \times \left[\frac{(\epsilon_1-\epsilon_2)(1-\beta^2\epsilon_2-\beta\sqrt{\epsilon_1-\epsilon_2\sin^2\theta})}{(1-\beta\sqrt{\epsilon_1-\epsilon_2\sin^2\theta})(\epsilon_1\cos\theta+\sqrt{\epsilon_1\epsilon_2-\epsilon_2^2\sin^2\theta})}\right]^2 . \quad (2.2)$$

Assuming electron crossing the boundary between ideal conductor and vacuum ($|\epsilon_1| \to \infty$, $\epsilon_2 = 1$), the equation (2.2) immediately yields the equation (2.1) [40].

Important consequence of the equation (2.2) is, that under the assumption for dielectric constant of medium (e.g. metal or plasma) to be $\epsilon = 1 - \omega_p^2/\omega^2$, where ω_p is the plasma-frequency of the medium and ω is the frequency of the emitted Transition Radiation, the equation (2.2) gives us the frequency dependence of the power spectrum. It can be shown [44], that there exists such cutoff frequency $\omega_c = \omega_p\gamma$ above which the power spectrum decreases as ω^{-4}, i.e. the radiator emits very weakly above ω_c. This gives us the *high-frequency cutoff* for the non-ideal materials unlike the equation (2.1), which is frequency independent.

Low-frequency cut-off emerges, when we introduce finite dimensions of the radiator. Diffraction Radiation from the edge of the finite radiator can be neglected under the condition $\rho \gg \lambda\gamma$, where ρ is the dimension of the radiator [40]. Otherwise, interference of the Transition Radiation and the Diffraction Radiation will limit the generation of long wavelength transition radiation resulting in the low-frequency cut-off.

It is important to note, that so far we have assumed, that the transition from one medium to another is step-like, which is only true for the cases, where the length of the boundary is smaller than the radiation *formation length* $L_f \sim \lambda\gamma^2$ [40]. In another words, imperfections such as roughness can be neglected if its characteristic dimensions are smaller than the formation length.

2.2 Electron Bunch Transition Radiation

So far we have only worked with one single electron moving perpendicularly to the boundary between two media. Usually from LWFAs we get electron bunches of charges at the order pC to nC (check chapter 1.5), which contains roughly up to $N \approx 10^{10}$ electrons. Following theoretical description is from [40].

We will consider the electron bunch propagating along the z-axis with N electrons emerging from a semi-infinite perfect conductor into the vacuum. We also assume, that the dimensions of the electron bunch are negligible to the observation distance, i.e. we can treat the bunch as a point source of Transition Radiation. As discussed previously, we will use step-like transition of dielectric constant. Electric current density created by the arbitrary electron bunch is [40]

$$\boldsymbol{J}_b(\boldsymbol{x}, t) = -ec \sum_{j=1}^{N} \boldsymbol{\beta}_j \delta(\boldsymbol{x} - \boldsymbol{r}_j - c\boldsymbol{\beta}_j t)\,, \tag{2.3}$$

where $\beta_j = \boldsymbol{v}_j/c$ is the speed of j-th electron, r_j is the position of j-th electron. Radiation emitted from the electron bunch passing through the boundary between two media is then given by [40]

$$\frac{\mathrm{d}^2 W}{\mathrm{d}\omega \mathrm{d}\Omega} = \frac{e^2}{4\pi^3 \varepsilon_0 c} \sum_{l=1}^{N} \sum_{j=1}^{N} (\mathcal{E}_{\parallel l} \mathcal{E}_{\parallel j} + \mathcal{E}_{\perp l} \mathcal{E}_{\perp j}) e^{i\Psi_j - i\Psi_l}\,, \tag{2.4}$$

where $\mathcal{E}_{\parallel j}$ ($\mathcal{E}_{\perp j}$) are the normalized electric field amplitudes parallel (perpendicular) to the radiation plane (given by z-axis and $\boldsymbol{k}$, where $\boldsymbol{k}$ is the wave number) given by [40]

$$\mathcal{E}_{\parallel j}(\theta, u_j, \psi_j, \phi_j) = \frac{u_j \cos\psi_j [u_j \sin\psi_j \cos\phi_j - (1+u_j^2)^{1/2} \sin\theta]}{[(1+u_j^2)^{1/2} - u_j \sin\psi_j \cos\phi_j \sin\theta]^2 - u_j^2 \cos^2\psi_j \cos^2\theta}\,, \tag{2.5}$$

$$\mathcal{E}_{\perp j}(\theta, u_j, \psi_j, \phi_j) = \frac{u_j^2 \cos\psi_j \sin\psi_j \sin\phi_j \cos\theta}{[(1+u_j^2)^{1/2} - u_j \sin\psi_j \cos\phi_j \sin\theta]^2 - u_j^2 \cos^2\psi_j \cos^2\theta}\,, \tag{2.6}$$

where $u = p/m_e c = \gamma\beta$ is the normalized momentum of the electrons, ψ_j is the angle between $j-$th electron propagation direction and z-axis, ϕ_j is the angle between the projection of electron propagation direction onto $x-y$ plane and x-axis.
Phase Ψ_j is given by [40]

$$\Psi_j = \boldsymbol{k}_\perp \cdot \boldsymbol{r}_{\perp j} + (\omega - \boldsymbol{k}_\perp \cdot \boldsymbol{v}_{\perp j}) z_j / v_{zj}\,, \tag{2.7}$$

where $\boldsymbol{k} = \frac{\omega}{c}(\sin\theta\cos\alpha, \sin\theta\sin\alpha, \cos\theta)$ is the wave number.
Using the equations (2.4), (2.5), (2.6) and (2.7), we can calculate the spectrum of the arbitrary electron bunch. These equations can be replaced by taking an average over the six-dimensions electron beam distribution $h(\boldsymbol{r}, \boldsymbol{p})$ [40] normalised as $h(\boldsymbol{r}, \boldsymbol{p})\mathrm{d}^3\boldsymbol{r}\mathrm{d}^3\boldsymbol{p} = 1$, and momentum distribution $g(\boldsymbol{p}) = \int h(\boldsymbol{r}, \boldsymbol{p})\mathrm{d}^3\boldsymbol{r}$.

The equation (2.7) then takes the form

$$\frac{\mathrm{d}^2W}{\mathrm{d}\omega\mathrm{d}\Omega} = \frac{e^2N}{4\pi^3\varepsilon_0 c}\left\{\int(\mathcal{E}_\perp^2+\mathcal{E}_\parallel^2)g(\boldsymbol{p})\mathrm{d}^3\boldsymbol{p}+ \right.$$
$$\left.(N-1)\left[\left|\int g(\boldsymbol{p})\mathcal{E}_\parallel F\mathrm{d}^3\boldsymbol{p}\right|^2+\left|\int g(\boldsymbol{p})\mathcal{E}_\perp F\mathrm{d}^3\boldsymbol{p}\right|^2\right]\right\}, \quad (2.8)$$

where F is the form factor defined as [40]

$$F = \frac{1}{g(\boldsymbol{p})}\int e^{-i\boldsymbol{k}_\perp\cdot\boldsymbol{r}_\perp}\mathrm{d}^2\boldsymbol{r}_\perp\int h(\boldsymbol{r},\boldsymbol{p})e^{-iz(\omega-\boldsymbol{k}_\perp\cdot\boldsymbol{v}_\perp)/v_z}\mathrm{d}z\,. \quad (2.9)$$

If we assume non-correlated electron position and momentum, we can write $h(\boldsymbol{r},\boldsymbol{p}) = f(\boldsymbol{r})g(\boldsymbol{p})$, which gives us the form factor as following

$$F = \int e^{-i\boldsymbol{k}_\perp\cdot\boldsymbol{r}_\perp}\mathrm{d}^2\boldsymbol{r}_\perp\int f(\boldsymbol{r})e^{-iz(\omega-\boldsymbol{k}_\perp\cdot\boldsymbol{v}_\perp)/v_z}\mathrm{d}z\,, \quad (2.10)$$

which is similar to the Fourier-transform of the spatial distribution of the electron bunch.
Assuming the Gaussian spatial beam distribution as
$f(r_\perp,z) = [(2\pi)^{3/2}\sigma_r^2\sigma_z]^{-1}\exp(-r_\perp^2/2\sigma_r^2 - z^2/2\sigma_z^2)$, where σ_z (σ_r) is the root-mean-square beam length (radius), the form factor $F = F_\perp F_\parallel$ then is [40]

$$F_\perp = e^{-(1/2)(\omega/c)^2\sigma_r^2\sin^2\theta}, \quad F_\parallel = e^{-(1/2)[\omega/(c\beta\cos\psi)]^2\sigma_z^2(1-\beta\sin\theta\cos\psi\sin\psi)^2}. \quad (2.11)$$

For almost divergence-less beam $\psi \ll 1$ we get $F_\parallel \approx \exp[-(\omega\sigma_z/v)^2/2]$.

We can immediately see, that for waves travelling in vacuum with wavelengths $\lambda = 2\pi c/\omega \gg \sigma_z$ we get $F_\parallel \approx 1$, thus the second term in the equation (2.8) dominates and scales with N^2. In such case we say, that the Transition Radiation is *coherent*, which is usually referred to as *Coherent Transition Radiation* (CTR).

When $\lambda \ll \sigma_z$, we get $F_\parallel \approx 0$ and the second term in the equation (2.8) is negligible, and only the first term, which scales with N, plays a role. In such case we say, that the Transition Radiation is *incoherent*, usually referred to as *Incoherent Transition Radiation* (ITR).

3. Relativistic electron beam diagnostics

In this chapter, 3 different types of detectors, their underlying principles, and their accompanying tools, used for Laser Wake-field Accelerators, are presented: Integrating Current Transformer for the bunch charge, Magnetic Spectrometer for energy spectrum, and Transition Radiation Detector for the length of the bunch.

3.1 Integrating Current Transformer

Integrating Current Transformer (ICT) is a non-invasive method (it affects the characteristics of the electron bunch minimally) of measuring the total charge of the generated electron bunch [45] $Q^{(\text{bunch})}$. Simplified schematic depiction is shown in Figure 3.1 below.

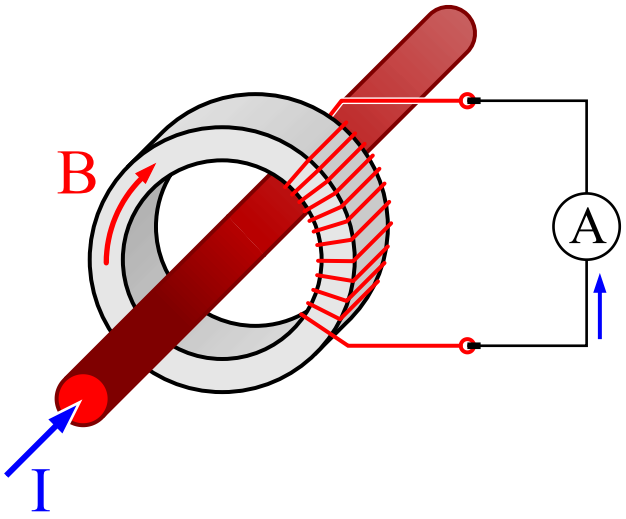

Figure 3.1: Schematics of the ICT. Reproduced from [46]

We can see from the equation (1.14), that the electric current $\boldsymbol{I}(\boldsymbol{r}, t)$ generated by a moving electron bunch (red rod) creates an axial magnetic field $\boldsymbol{B}(\boldsymbol{r}, t)$ passing through the coil (red line wrapped around the gray cylinder). Since this electric current is time-dependent, the magnetic field is also time-dependent. Following from the equation (1.13), the time-change in the magnetic field induces the electric current in the coil, which can be measured by the amperemeter **A**. Integrating the current from the ampermeter over time gives us the charge $Q^{(\text{integrated})}$, which is proportional to the charge of the electron bunch $Q^{(\text{bunch})}$, i.e. $Q^{(\text{integrated})} \propto Q^{(\text{bunch})}$. The constant of proportionality is the matter of the geometry and characteristics of the experimental setup, and has to be calibrated. Undesired electromagnetic pulses (EMPs) have to be also taken into account, since the connecting cables or ICT itself can pick-up these EMPs and the signal can become corrupted and the expected $Q^{(\text{bunch})}$ can be excessively innacurate [47][48].

3.2 Magnetic Spectrometer

The electron energy (charge) spectrum $\mathrm{d}N/\mathrm{d}E$ ($\mathrm{d}Q/\mathrm{d}E$) can be measured using the dipole magnetic spectrometer. The trajectory of the electron passing through the magnetic field B at speed v is bent into a circular path by the Lorentz force. Assuming the electron is traveling perpendicularly to the magnetic field B, the radius R of the circular path of the electron can be expressed as

$$R = \frac{m_e \gamma v}{eB} \,. \tag{3.1}$$

We can immediately see, that electrons with higher energies are bent less than electrons with lower energies. Consequently, electrons from the electron bunch passing through the magnetic field will be dispersed according to their energy, i.e. magnetic field turns energy distribution into a spatial distribution. By inserting the image plane (e.g. scintillator) into the electron trajectories, we can detect this distribution.

Electron trajectories for electrons with Lorentz factors ranging from $\gamma = 100$ to $\gamma = 1000$ (energies ranging from 51 MeV to 511 MeV) passing through the magnetic field $B = 1$ T (shown by the blue rectangle) with length 20 cm and width 5 cm hitting the image plane (red line) are depicted in Figure 3.2 below.

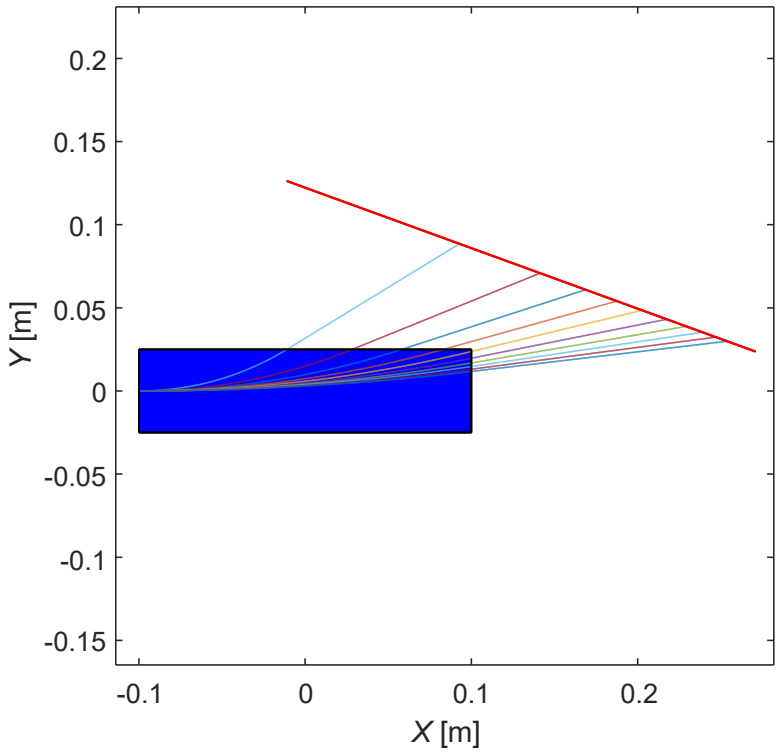

Figure 3.2: Trajectories of electrons with different energies passing through the magnetic field (blue rectangle) and hitting the image plane (red line)

3.2.1 Electron pointing

All the electrons in Figure 3.2 entered the magnetic field perpendicularly to the front side of the magnetic field, i.e. they were initially moving parallel to the x-axis. However, in the real case, electrons enter the magnetic field at an oblique angle. This phenomenon is called the *electron pointing*. While in the ideal case of zero electron pointing, each position on the image plane corresponds to the unique energy, in the real case of non-zero electron pointing, each position can correspond to more than one energy due to the fact, that the electron with the energy E and the incident angle θ_1 can hit the image plane at the same position as the electron with the energy $E + \Delta E$ and the incident angle θ_2.

In the figure 3.3, two electrons with different energies and different electron pointing are shown. The electron with energy 102 MeV ($\gamma \approx 200$) entered the magnetic field at an angle $\theta = 20$ mrad (with respect to the normal of the surface of the magnetic field, i.e. with respect to x-axis in this case, clockwise angle with respect to x-axis is positive) and the electron with energy 115 Mev ($\gamma \approx 225$) entered at the angle $\theta = -20$ mrad.

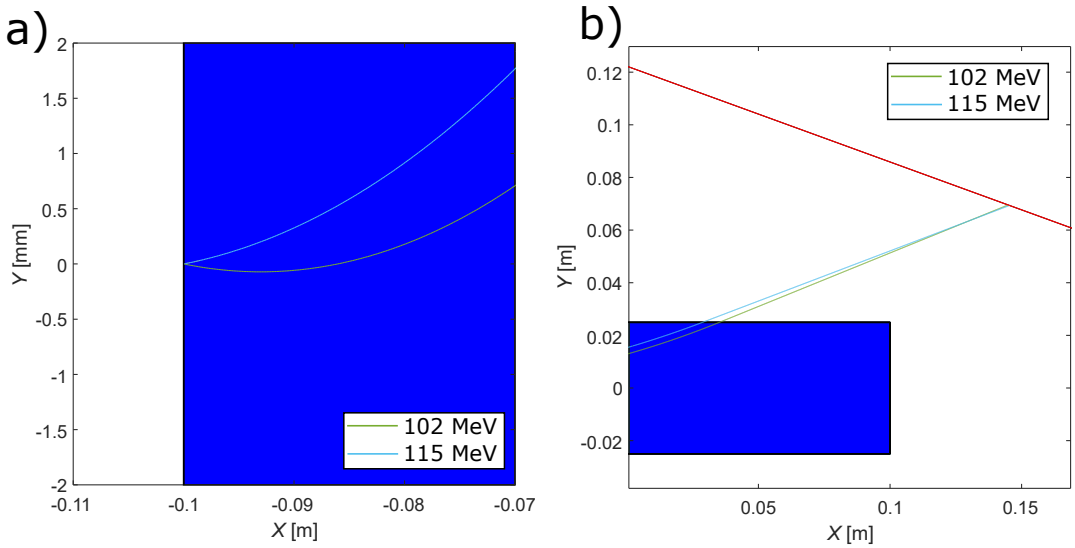

Figure 3.3: Electrons with two different energies and pointing angles pass through magnetic field. a) trajectories at the front of the magnetic field, b) trajectories after exiting the magnetic field

In this case, it is unclear what energy does the given position correspond to. Or alternatively, we can have a mono-energetic bunch with non-zero pointing, which will appear to be a polyenergetic bunch without electron pointing after hitting the image plane, because electrons entering perpendicularly to the magnetic field front will hit image plane at a spot, which corresponds to zero-incidence angle electron with different energy.

It is therefore useful to define the *resolution* of the spectrometer as

$$\frac{\Delta E}{E} = \frac{E_{max} - E_{min}}{E}, \tag{3.2}$$

where E is the energy of the electron, E_{min} (E_{max}) is the minimum (maximum) energy of the *zero* pointing electron corresponding to the spot hit by the *non-zero*

pointing electron with the said energy E. In another words, ΔE is the range of energies, which non-zero pointing mono-energetic bunch appears to contain after hitting the image plane. The example of resolution is shown in Figure 3.4, where 3 electrons with the same energy $E \approx 102$ MeV ($\gamma = 200$) and different electron pointing hit the image plane at 3 different spots.

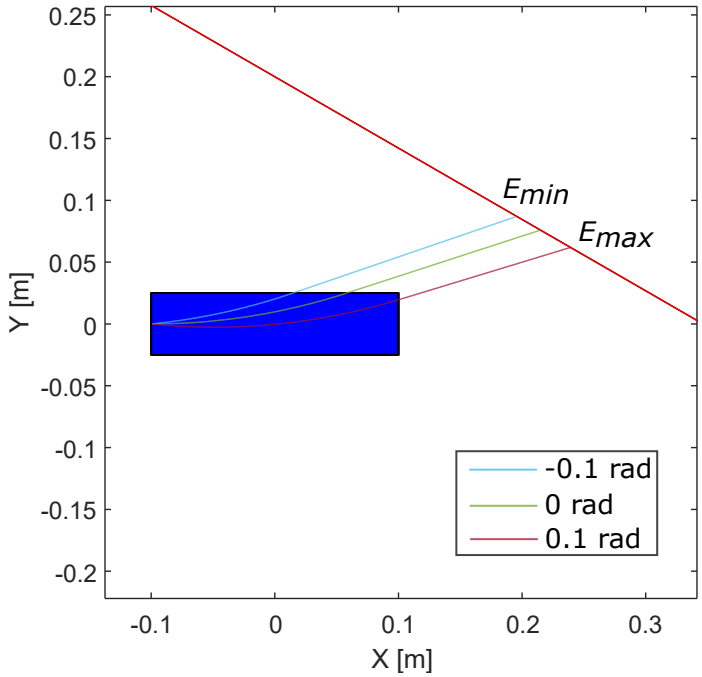

Figure 3.4: Mono-energetic bunch with 3 electrons with different electron pointings

In this case, the minimum energy was $E_{min} = 81$ MeV, the maximum energy was $E_{max} = 127$ MeV, therefore, the resolution is approximately $\Delta E/E \approx 45\%$.

3.2.2 Magnetic Spectrometer App

In the figure 3.2, the boundary between the magnetic field and the rest of the space is step-like. However, in the real case, the magnetic field is inhomogeneous and does not have a step-like boundary. In order to be able to predict the trajectories of electrons in the real magnet, its magnetic field has to be directly measured and compared with homogeneous idealisation with step-like boundary.

For the purpose of the numerical calibration of the Magnetic Spectrometer, the app *Magnetic Spectrometer App* was developed using MATLAB App Designer created by MathWorks®. Its main user interface (UI) is shown in Figure 3.5 below.

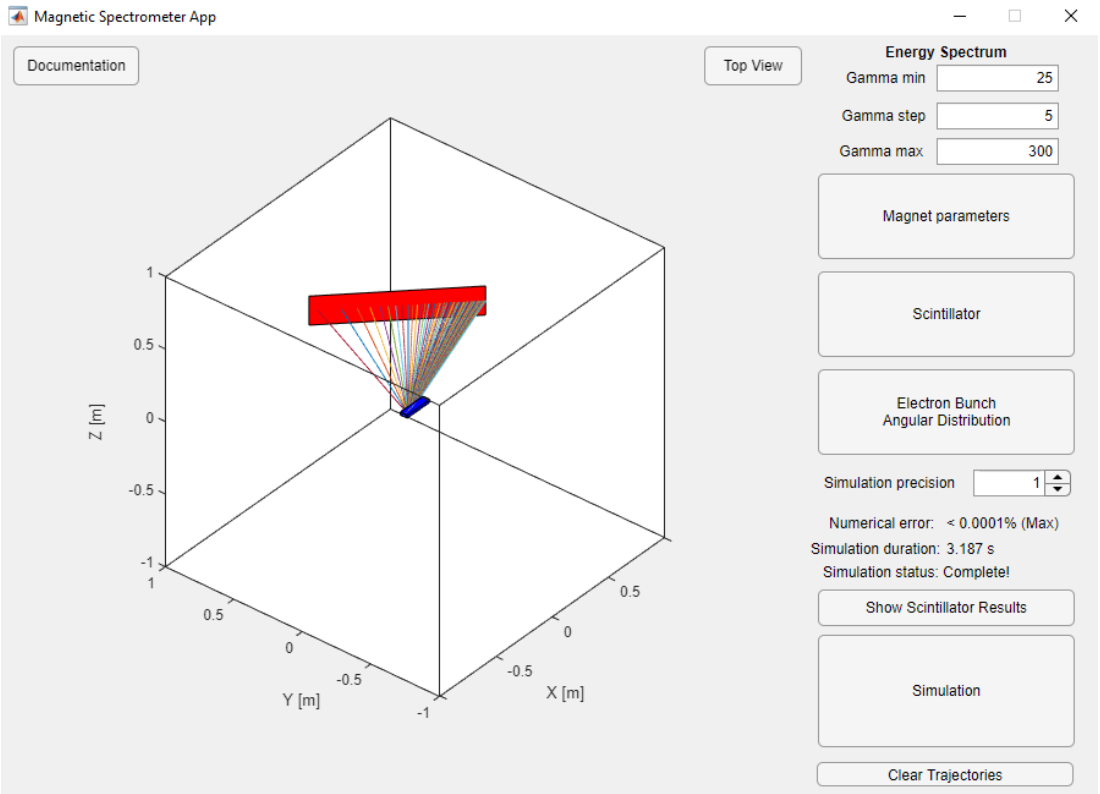

Figure 3.5: UI of the Magnetic Spectrometer App for an arbitrary custom experimental setup and electron bunch with zero pointing

This app enables its user to easily predict and calibrate the magnetic spectrometer by entering the parameters of the given experimental setup.

The app uses the numerical method *MidPoint* [49] to numerically solve the differential equation for the electron motion in magnetic field for different electron energies. Part of the code used for the numerical solution using this method is shown in the section A.2.

The button *Magnet Parameters* gives the user the option to choose between homogeneous magnetic field of given dimensions, or to use the custom data from the measurement of the magnetic field of the dipole magnet (corresponding window shown in Figure 3.6, left). The *Scintillator* button offers the option to customize the position and dimensions of the image plane (corresponding window shown in Figure 3.6, right).

The *Electron Bunch Angular Distribution* controls the electron pointing (corresponding window shown in Figure 3.7).

The user can also see the maximum numerical error of the simulation based on the maximum change of the Lorentz factor from all the electrons, since the Lorentz factor is proportional to the electron's energy, which conserves for the particle travelling through the magnetic field.

The *Simulation* button starts the simulation for the given parameters. To visualize the results of electron detections on the image plane, the *Show Scintillator Results* button can be used (the result for the setup shown in Figure 3.5 is shown in Figure 3.8).

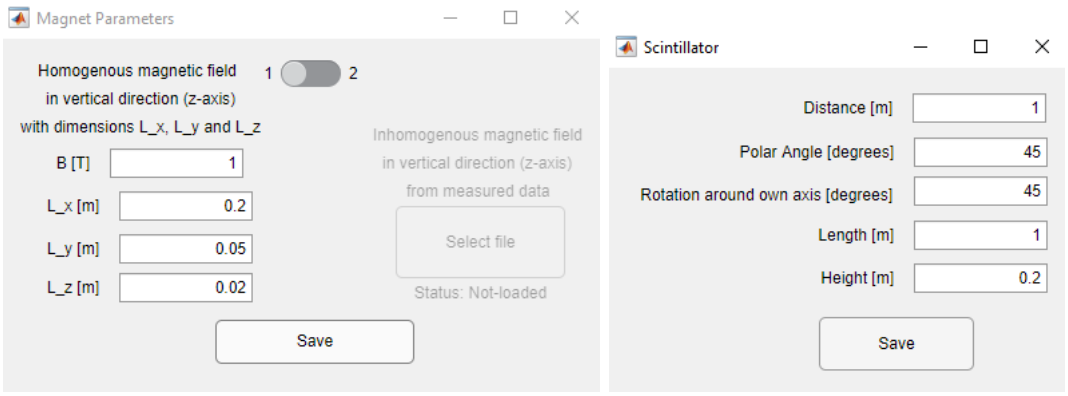

Figure 3.6: *Left*: The *Magnet Parameters* window for magnetic field settings. *Right*: The *Scintillator* window for image plane settings

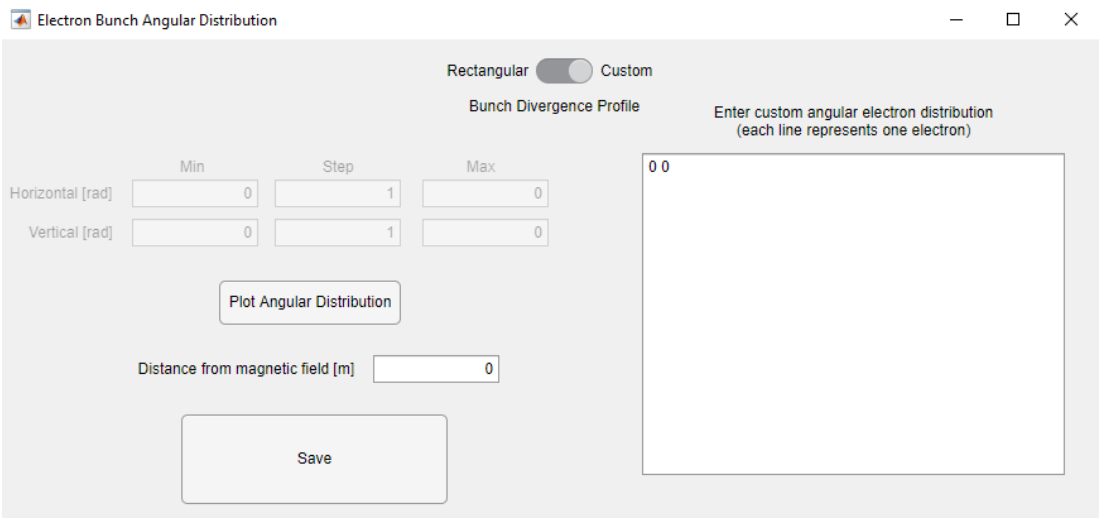

Figure 3.7: The *Electron Bunch Angular Distribution* window for electron beam pointing settings

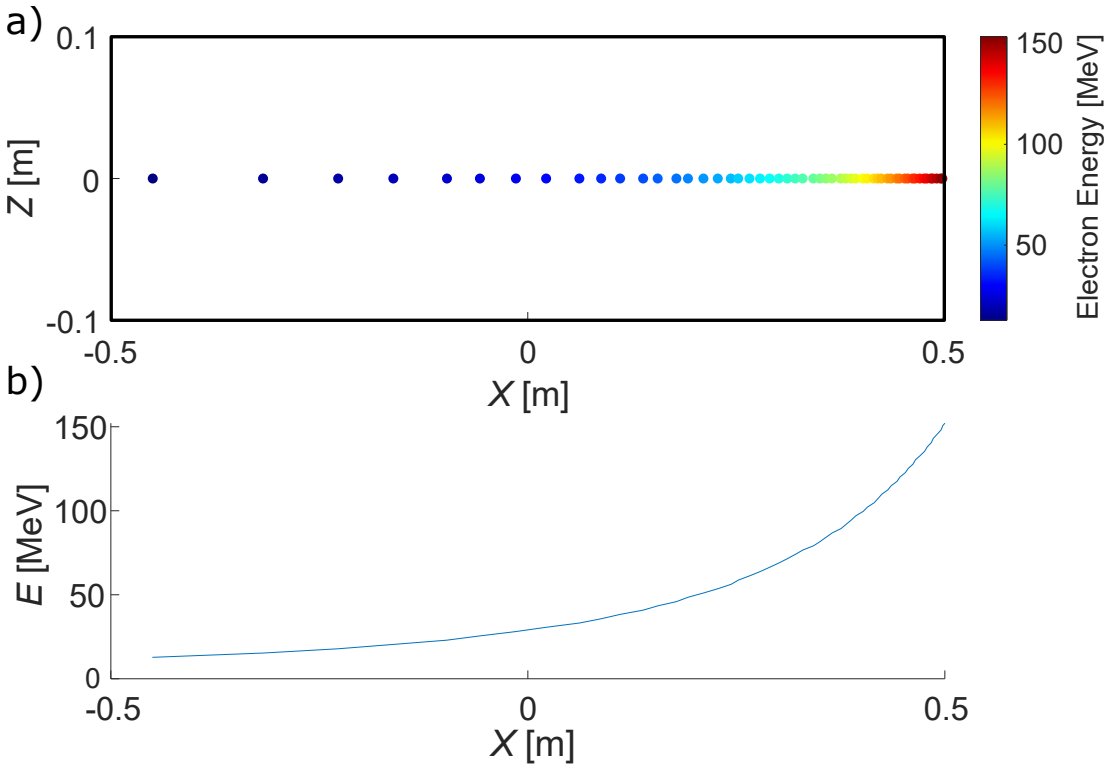

Figure 3.8: *Scintillator Results* for the arbitrary setup shown in Figure 3.5. a) Detections observed on the scintillating screen colored according to their energy shown on the colorbar on the right. b) Dependence of zero pointing electron energy on the horizontal position on the scintillator

Resolution of the spectrometer is also calculated by pressing the *Scintillator Results* button, but since the bunch in the example does not have electron pointing, the resolution would be 0% (ideal resolution), and thus it is not necessary to be shown (case of non-zero resolution will be shown in the section 4.2).

3.3 Transition Radiation Detector

As shown in chapter 2.2, the TR spectrum is directly connected to the spatial distribution via the *Form Factor* given by the equation (2.9) or (2.10). If we assume a negligible transverse momentum ($\boldsymbol{v}_\perp \ll 1$), the equation (2.10) then is

$$F = \int f(\boldsymbol{r}) e^{-i\boldsymbol{k}\cdot\boldsymbol{r}} \mathrm{d}^3 r \,, \tag{3.3}$$

which is the Fourier Transform of the spatial distribution of the electron bunch. Hence, we can obtain the spatial distribution of the bunch by measuring the spectrum of the TR.

As an example, we'll assume very narrow ($\sigma_r \ll \lambda$, $F_\perp \approx 1$) electron bunch with Gaussian longitudinal distribution $f_\parallel(z) = [\sqrt{2\pi}\sigma_z]^{-1} \exp(-z^2/2\sigma_z^2)$. Corresponding TR spectra for different σ_z calculated via the equation (2.4) observed at angle $\theta = 1/\gamma$ are shown in the figure 3.9.

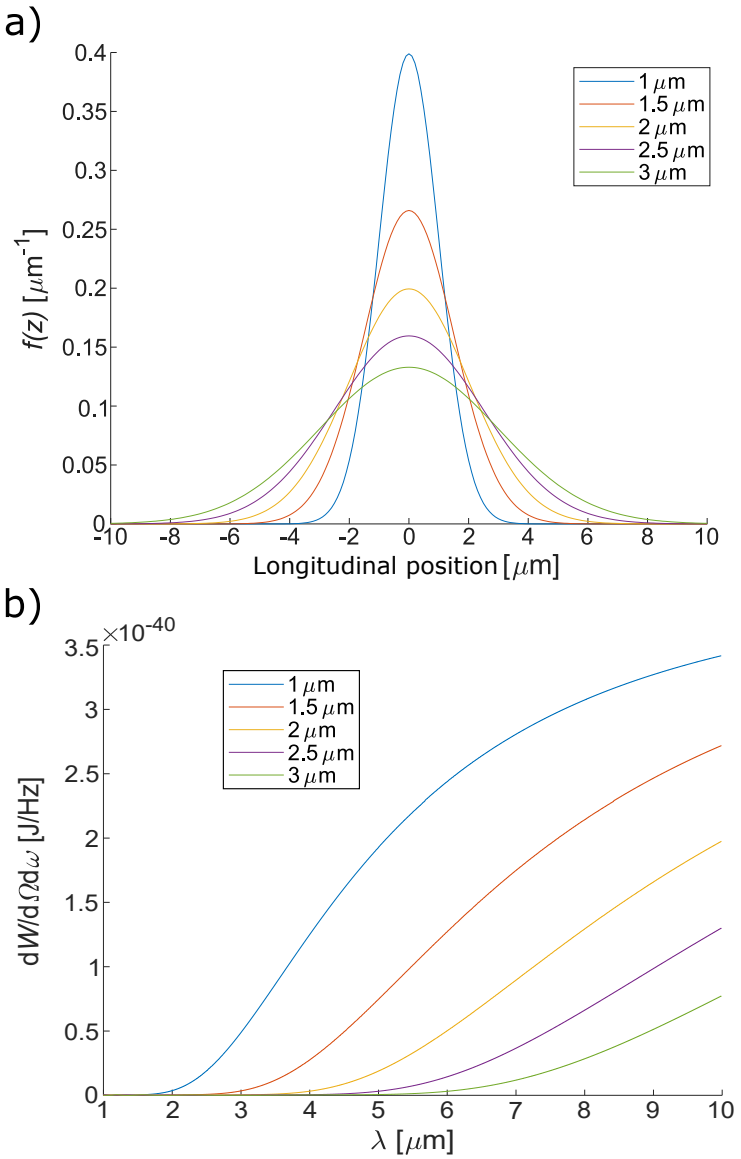

Figure 3.9: Transition radiation spectra for Gaussian beams with different σ_z. a) Beam profiles, b) Corresponding spectra

We can see, that for each electron bunch, the intensity of transition radiation increases dramatically when the wavelength λ of the emitted radiation becomes greater than the σ_z, as we described in the chapter 2.2. Figure 3.9 shows how the shape and size of the bunch affects its corresponding spectrum.

Due to the high no-linearity of the electron injection process, internal substructures can be produced in the bunch [50]. While in the examples shown in the Figure 3.9 the length of the bunch was in order of $\sim \mu m$, created substructures can have lengths in order of $\sim 100nm$, which enable the electron bunch to radiate CTR in the optical spectrum, called *Coherent Optical Transition Radiation* (COTR). COTR is one of the first indicators of substructures smaller than the bunch envelope.

In the Figure 3.10, five consecutive Gaussian smaller bunches separated by 200 nm, each with same rms σ, are shown together with their corresponding spectra. For each spectrum, the σ was changed.

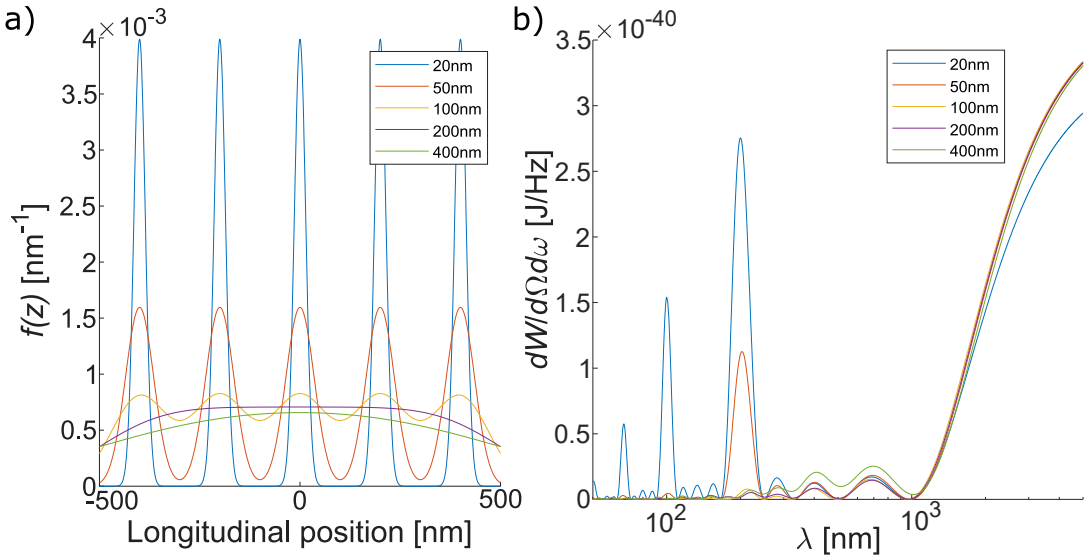

Figure 3.10: Effect of internal substructures on Transition Radiation.
a) Longitudinal distribution, b) Corresponding transition radiation spectra

From figure 3.10 we can see that the introduction of substructures results in CTR with wavelengths smaller ($\sim$ nm) than the bunch envelope ($\sim \mu$m) with several spectral peaks (harmonics) separated by frequency that is inversely proportional to the length of substructures.

Generally, substructures in the main bunch create CTR at wavelengths smaller than the length of the bunch envelope. From intensity spikes in the optical region we can obtain the internal structure of the bunch. Therefore, emission of COTR implies the existence of nanometer-scale substructures.

Direct reconstruction of the electron-bunch spatial distribution from the TR spectrum via the Inverse Fourier Transform is impossible, since the phase information is lost by measuring the TR spectrum via its intensity. This problem is called the *phase problem*. Different phase-retrieval algorithms have been developed over the years to tackle this problem. For example The Gerchberg-Saxton algorithm was designed to reconstruct the phase information from the intensity measurement [51]. Another example is the "Bubblewrap" algorithm, which was also explicitly used to reconstruct electron bunch spatial distribution from CTR measurement [52].

4. Experimental Setup

In this chapter, experimental equipment planned to be used in the upcoming experiment will be shown. Experiment will be held at ELI-Beamlines facility in Dolní Břežany (Czech Republic), which is a part of European Extreme Light Infrastructure project [53].

Figure 4.1: Laser L3 HALPS. Reproduced from [53]

Drive laser pulse from the Sapphire petawatt class Laser L3 HALPS has the duration $\tau_{(\mathrm{FWHM})} = 28$ fs, peak power up to 1 PW, total energy of the pulse $W = 30$ J, and focused beam radius $w_0 = 14$ μm. It gives the intensity up to $I_0 \doteq 1.6 \cdot 10^{20}$ W/cm^2. The illustration of laser wakefield electron acceleration at ELI-Beamlines is shown on the figure 4.2.

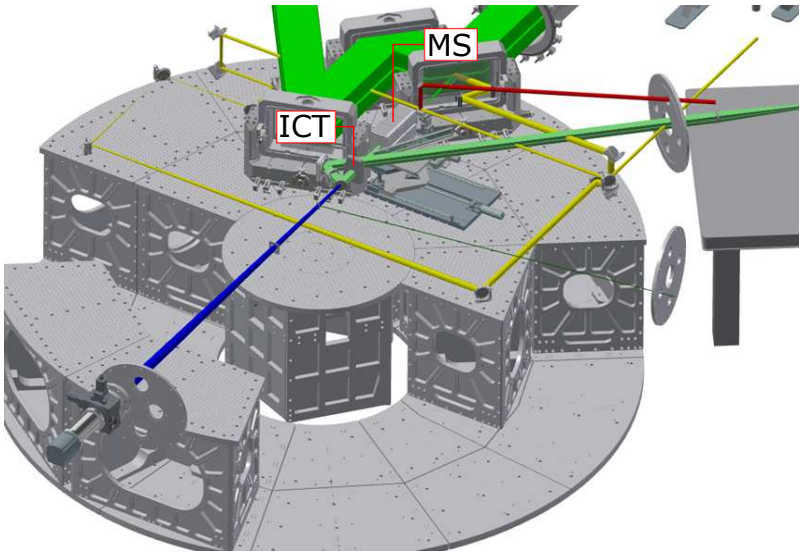

Figure 4.2: Illustration of laser wakefield electron acceleration at ELI-Beamlines

Figure 4.2 shows the experimental setup of electron and betatron X-ray generation based on LWFA in Experimental hall E3 in the Plasma Physics Platform (P3). For the generation of electrons and betatron x-ray, the ELI beamlines L3 laser beam (10 J, 30 fs, repetition rate: up to 10 Hz, *large green*) is delivered onto the focusing spherical mirror (focal length of 500 cm) by a mirror with holes, thus the beam can be impinging the focusing mirror perpendicularly and is focused back through the hole into the gas jet. The choice of the focal length is defined to reach a laser strength parameter sufficiently high ($a_0 \sim 4$).

4.1 Integrating Current Transformer

Integrating Current Transformer (ICT) is labeled in figure 4.2 as **ICT**. The ICT used in the experiment will be *The Turbo-ICT-VAC-055 current sensor* with a dynamic range of 80 dB capable of resolving fC scale pulsed charges manufactured by the company *Bergoz Instrumentation* [54]. It is compatible with with vacuum to 10^{-7} mbar. The illustration from the official technical drawing provided by the manufacturer is shown in figure 4.3 below [54].

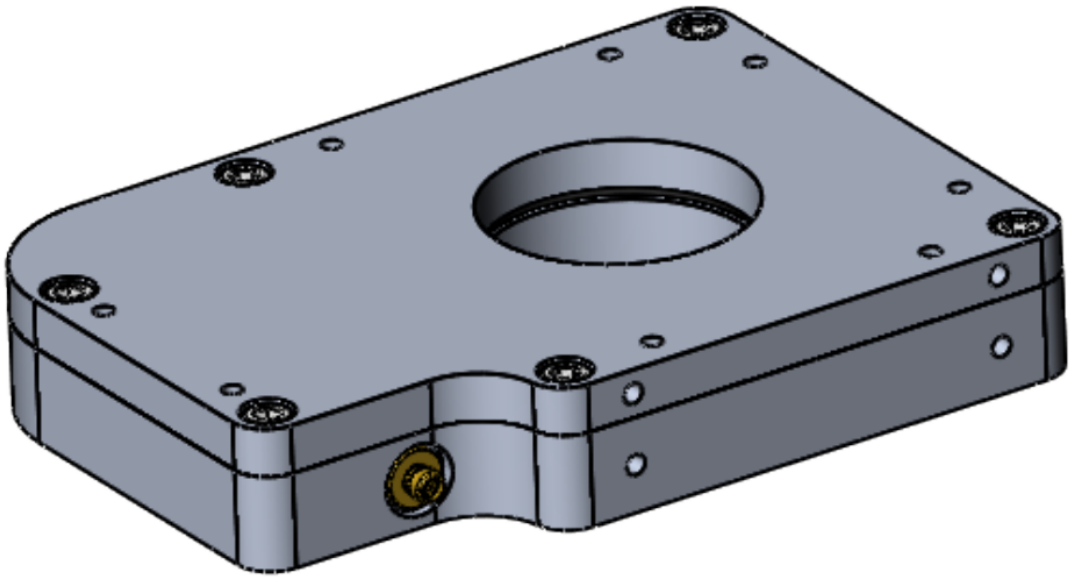

Figure 4.3: Integrating Current Transformer *The Turbo-ICT-VAC-055*. Reproduced from [54]

4.2 Magnetic Spectrometer

The Magnetic Spectrometer is labeled in figure 4.2 as **MS**. Illustration of the magnetic spectrometer setup is shown in figure 4.4.

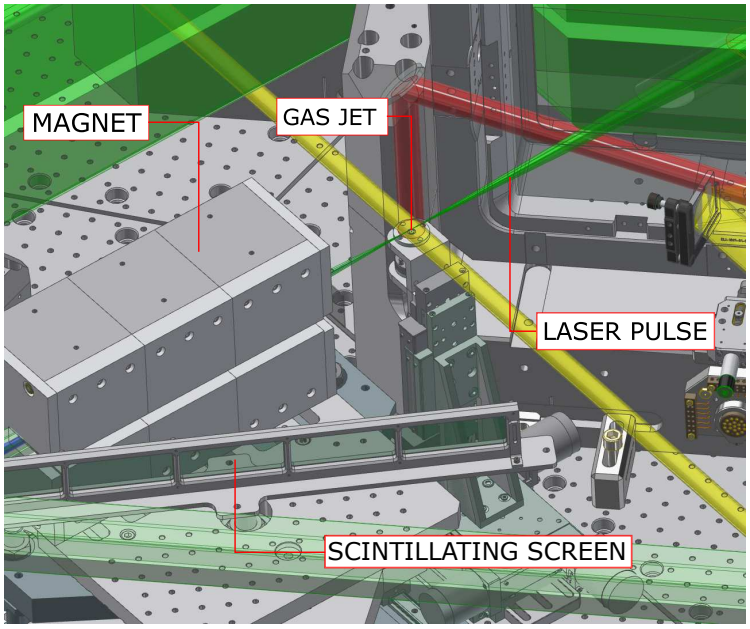

Figure 4.4: Magnetic Spectrometer Illustration

For the purposes of the magnetic spectrometer, custom permanent magnet was made at ELI-Beamlines. Its magnetic field was measured by a *Gaussmeter GM08 DC* manufactured by the company *Hirst Magnetic Instruments Ltd.* The Gaussmeter measured the projection of the magnetic field of the magnet onto the z-axis. The probe of the Gaussmeter was controlled by the robot using the Python script and local-host web browser interface. The magnet is shown on the figure 4.5.

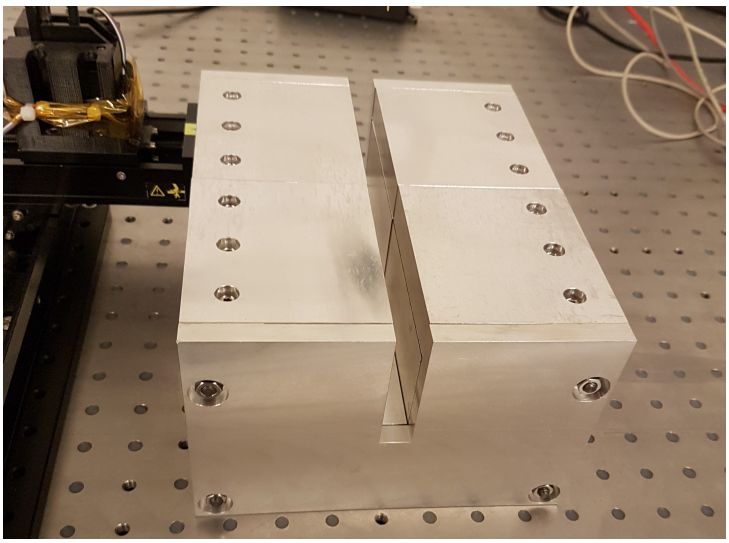

Figure 4.5: Dipole magnetic spectrometer with the peak magnetic field of up to 1 T

For the increased accuracy of numerical calculations, magnetic field was additionally measured 2 cm beyond its edges. The resolution of the measurement (distance between two points in a grid) was 2 mm.

The cross-section of the measured magnetic field is shown on the figure 4.6. The length of the measured magnetic field was 254 mm, width was 12 mm and the height was 80 mm. Magnet itself was 220 mm long and 45 mm wide.

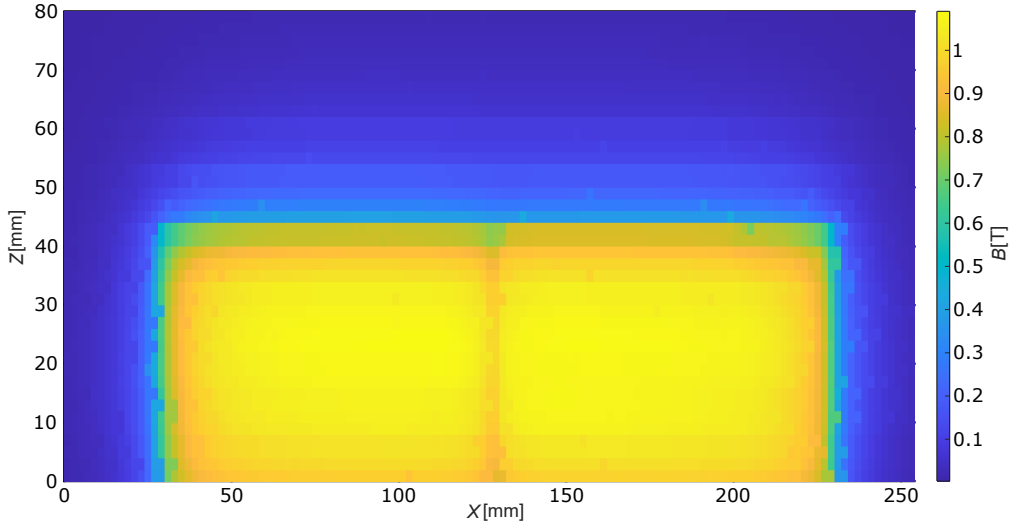

Figure 4.6: Cross-section of the measured magnetic field of the magnet with resolution 2mm

We see that the magnetic field of the magnet is nearly homogeneous and the idealisation of the homogeneous magnetic field of 1T is sufficient. Comparison of the simulation with 1T homogeneous magnetic field and the simulation with inhomogeneous magnetic field from the the measured data is shown on the figure 4.7.

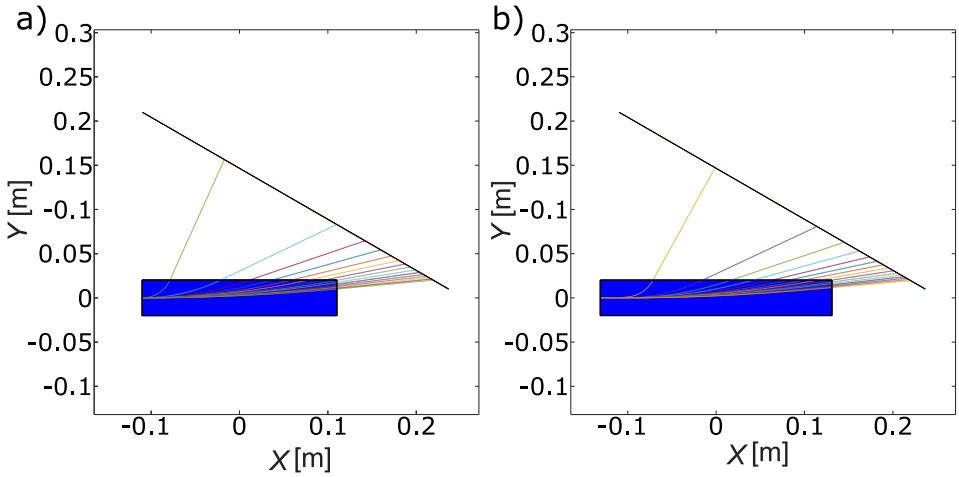

Figure 4.7: Comparison of the calculations with homogeneous 1T magnetic field and the real magnetic field.
a) Homogeneous 1T magnetic field, b) Real magnetic field

Both results are nearly identical, thus we can perform the calibration with idealisation of homogeneous 1T magnetic field of the setup shown on the figure 4.4. To calculate the resolution of the magnetic spectrometer according to the definition in the section 3.2, the bunch with energies from 10 MeV to 766 MeV (γ from 20 to 1500 with step 0.1) and divergence 20 mrad is used. Totally, the 45000 electron trajectories were calculated. The results are shown in Figure 4.8.

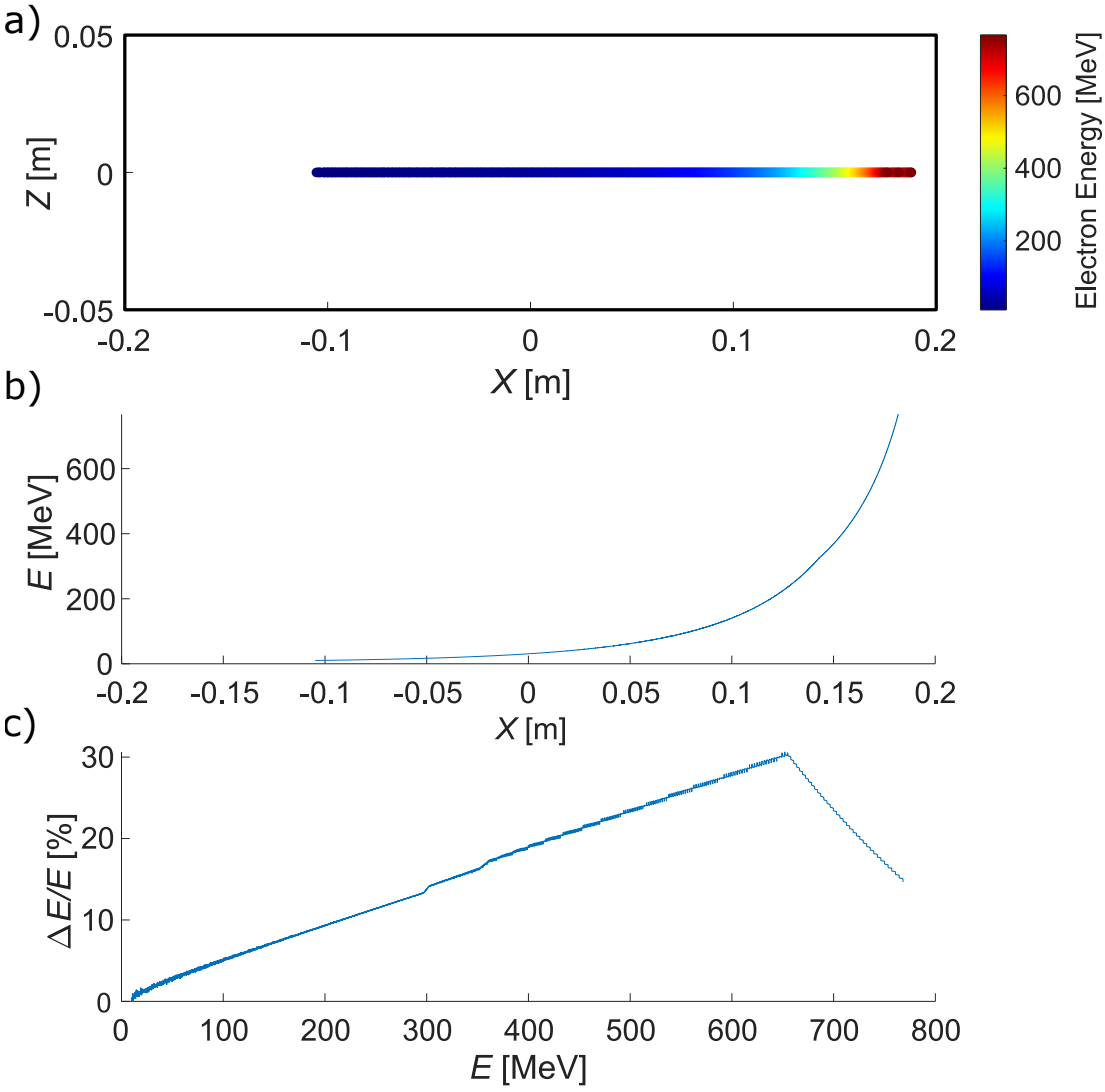

Figure 4.8: Numerical calibration of Magnetic Spectrometer. a) Detections observed on the scintillating screen colored according to their energy by the colorbar on the right. b) Dependence of zero-pointing electron energy on the horizontal position on the scintillator. c) Dependence of the resolution on the electron energy

The peak of resolution at energies around 650 MeV corresponds to electrons passing through the area around the corner of the magnet.

4.2.1 Scintillator screen

For the image plane, 3 different devices were chosen: *YAG:Ce* scintillator developed by the company *CRYTUR* [55] , *YAG:Ce* scintillator developed by the company *Advatech UK* [56], and the *Lanex Screen* developed by the company *Carestream* [57].
Sensitivity of those scintillators was tested. Each device was irradiated with the same X-Ray tube. Resulting emission was captured by the HD CCD camera (4096x3000 pixels) with bandpass filter 550 ± 40 nm and analysed with MATLAB script. For each measurement, the background picture with the X-ray source turned off was taken, followed by turning on the X-ray source and taking the picture of the emission. After subtracting the background picture from the measurement, the peak was found as the area where value of the gray-scale intensity increased over a certain threshold (90% of the maximum value), followed by plotting the RGB values horizontally along the center of the peak. Results are in Figure 4.9.

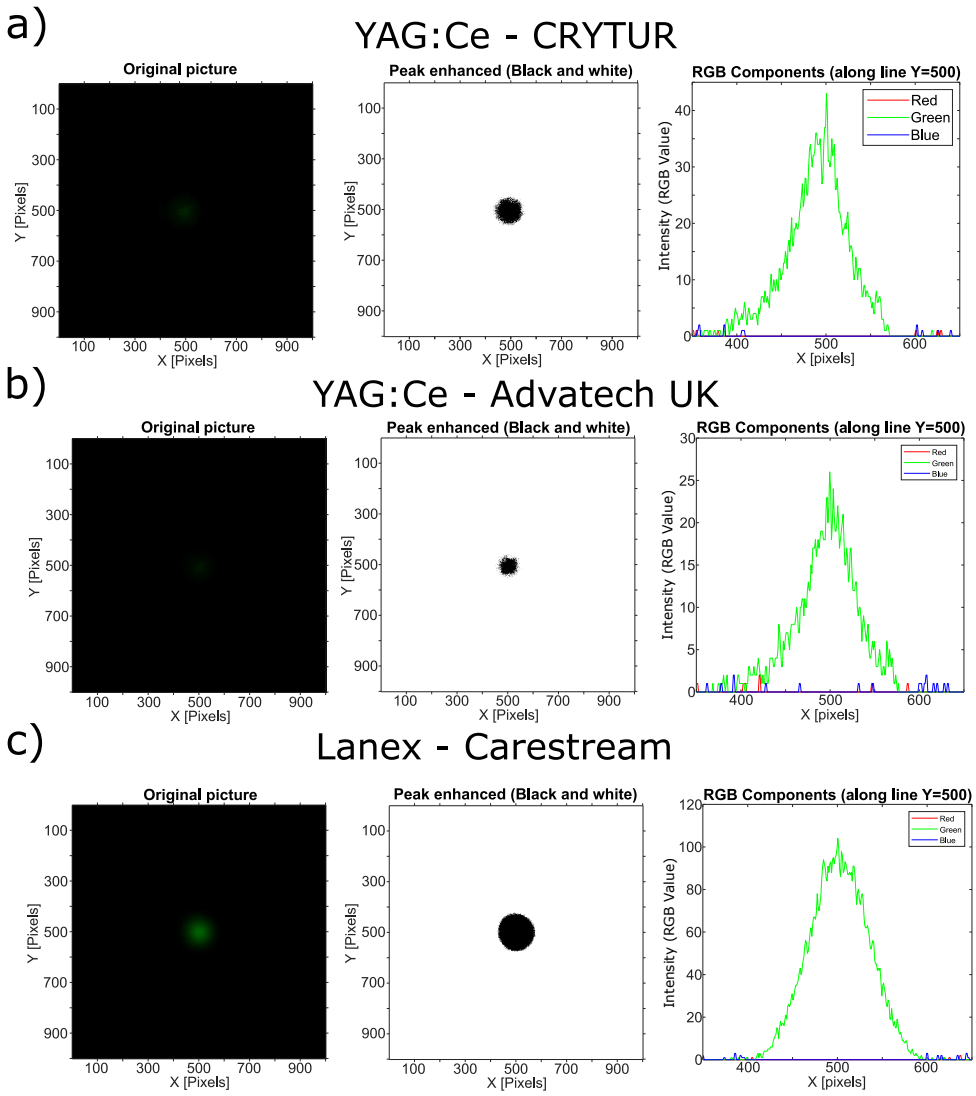

Figure 4.9: Emissivity analysis of the image plane devices.
a) YAG:Ce scintillator made by CRYTUR. b) YAG:Ce scintillator made by Advatech UK c) Lanex scintillator made by Carestream

From the figure 4.9 it is clear that the Lanex screen by Carestream emits the strongest signal and therefore is the best candidate. However, main disadvantage of the Lanex screen is outgassing, which can contaminate the high quality vacuum.

4.3 Transition Radiation Detector

In sections 2.2 and 3.3 we have shown that the boundary between CTR and ITR is directly proportional to the length of the bunch. This implies, that since we want to determine the length of the bunch from the CTR spectrum, we have to cover the radiation wavelengths greater than or equal to the length of the bunch of our interest. For example, if we want to inspect 2 μm long bunch, we have to measure spectrum for the wavelengths greater than or equal to 2 μm. Additionally, if the diagnostics of electron bunch substructures (microbunches) few hundreds nanometers long are of our interest, we have to also measure the visible spectrum or even UV.

These conditions enable us to determine the detection bandwidth of our Transition Radiation Setup. As discussed in the section 1.6, the length of the bunch is approximately the first half of the accelerating cavity, i.e. $\lambda_p/2$, which is typically at the order of $\sim \mu$m. Together with the need for the measurement of the substructures, our TR detector bandwidth should have the bandwidth 350nm-12μm.

Design proposal of the transition radiation detector setup including also the Magnetic Spectrometer and ICT is shown on the figure 4.10 below.

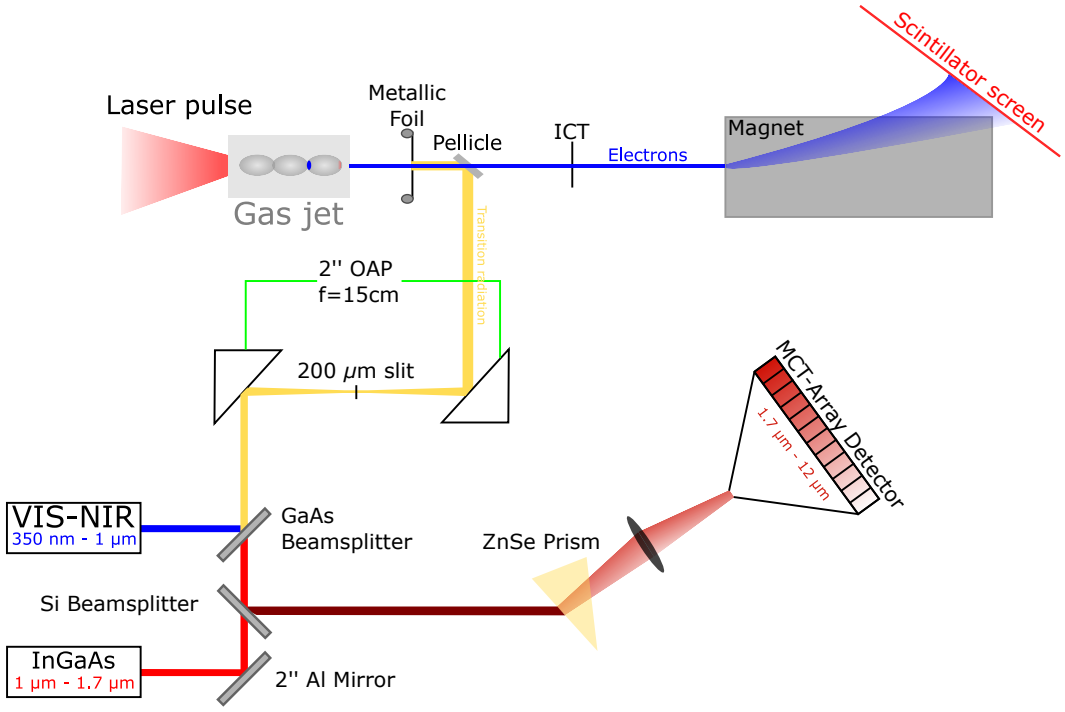

Figure 4.10: Experimental design of the Transition Radiation Detector setup

Electron bunch emerging from the *Gas Jet* passes through the *Metallic foil* and TR is emitted (yellow line). From the condition discussed in the section 2.1.1, to suppress the effect of diffraction radiation, the dimension of the radiator ρ must satisfy the condition $\rho \gg \lambda\gamma$. Since the maximum wavelength of TR of our interest is 12 μm and maximum Lorentz factor is $\gamma = 1500$, the radiator should be larger than 18 mm. *High-frequency cutoff* at frequency $\omega_c = \omega_p\gamma$ in case of aluminum ($\hbar\omega_p = 15$eV [58]) for $\gamma = 20$ is $\approx 4.5 \cdot 10^{16}$ Hz, which corresponds to

the wavelength $\lambda \approx 42$ nm well below the wavelengths of our interest and thus we don't have to consider calculations for imperfect conductor in case of aluminium. Transition radiation is then separated from the electron beam via a coated pellicle. TR from the back of the pellicle may interfere with the transition radiation from the metallic foil, and therefore the distance between the metallic foil and pellicle has to be smaller than the *formation length* [59] to mitigate this effect.

Electrons propagate further through the *ICT*, where their charge is measured, and the Magnetic Spectrometer, where their energy spectrum is determined. For determining the electron pointing, additional Lanex Screen can be positioned in front of the magnet.

Transition radiation propagates perpendicularly to the path of the electrons towards two *Off-axis parabolic mirrors* with 200 μm slit for spatial filtering. Transition radiation beam then propagates through the *GaAs beamsplitter*, which separates wavelengths below and above 1 μm [60]. Wavelengths below 1 μm are measured by the commercial *VIS-NIR Spectrometer* based on linear silicon CCD array with detection bandwith 350 nm-1 μm, optical resolution 1.33 nm (FWHM) and entrance slit 25 μm [61], manufactured by the company *Ocean Optics*.

Wavelengths above 1 μm propagate forward and the beam is again split on *Fused Silica Beamsplitter*, which splits the beam into the portions below and above 1.7 μm. Portion below the 1.7 μm reflects off the 2″ aluminium mirror and is measured by the commercial *InGaAs* detector manufacted by the company *Ocean Optics* with bandwidth 970 nm - 1.7 μm, optical resolution 10 nm (FWHM), and entrance slit 25 μm [62].

Rest of the beam with the wavelengths above the 1.7 μm propagate towards the *ZnSe* prism. *ZnSe* is good candidate for dispersing the infrared radiation due to its high transmission in the spectrum 0.6μm-15μm [63]. The transition radiation is dispersed by this prism and focused on the *Mercury-Cadmium-Telluride Array Detector* with 128x128 pixels and good overall sensitivity in the spectrum 1.7 μm-12 μm [64].

Conclusion

In this thesis, I have presented a summary of available literature on the theory of Laser wakeField accelerators and transition radiation. In **Chapter 1**, I have described the underlying principles behind LWFA, its properties, limitations, and current experimental results. In **Chapter 2**, I have summarized theory and performed numerical simulations of transition radiation. I have evaluated properties of its spectrum, its limitations outside of idealistic conditions, and shown how it is useful for determining the length of electron bunches emerging from LWFA. In **Chapter 3**, 3 types of relativistic electron beam diagnostics were presented. Integrating Current Transformer for determining the charge of the electron bunch, Magnetic Spectrometer for measuring its energy spectrum, and principle behind Transition Radiation Detector was described. Most importantly, the Magnetic Spectrometer App was developed for quick and simple calibration of the Magnetic Spectrometer. In **Chapter 4**, the experimental setup for LWFA with given laser parameters and aforementioned detectors were presented for the experiment, which will be performed in Dolní Břežany, Czech Republic. Integrating Current Transformer used for the setup was shown. The magnetic field measurement for the Magnetic Spectrometer was discussed and compared to homogeneous idealization, and calibration of the experimental setup for Magnetic Spectrometer via Magnetic Spectrometer App was performed. Lastly, the design of the future Transition Radiation Detector was proposed, each of its components was discussed.

Bibliography

[1] J. J. Thomson M.A. F.R.S. Xl. cathode rays. *The London, Edinburgh, and Dublin Philosophical Magazine and Journal of Science*, 44(269):293–316, 1897.

[2] Professor E. Rutherford F.R.S. Lxxix. the scattering of α and β particles by matter and the structure of the atom. *The London, Edinburgh, and Dublin Philosophical Magazine and Journal of Science*, 21(125):669–688, 1911.

[3] Professor Sir E. Rutherford F.R.S. Liv. collision of α particles with light atoms. iv. an anomalous effect in nitrogen. *The London, Edinburgh, and Dublin Philosophical Magazine and Journal of Science*, 37(222):581–587, 1919.

[4] Address of the president, sir ernest rutherford, o. m., at the anniversary meeting, november 30, 1927. *Proceedings of the Royal Society of London. Series A, Containing Papers of a Mathematical and Physical Character*, 117(777):310, 1928.

[5] G. Gamow. The quantum theory of nuclear disintegration. *Nature*, 122(3082):805–806, 1928.

[6] George Gamow. Quantum theory of the atomic nucleus. *Zeitschrift für Physik*, 51:204–212, 1928.

[7] Ronald W. Gurney and Edw. U. Condon. Wave mechanics and radioactive disintegration. *Nature*, 122(3073):439–439, 1928.

[8] John Cockcroft and Ernest Walton. Experiments with high velocity positive ions.—(i) further developments in the method of obtaining high velocity positive ions. *Proceedings of the Royal Society of London. Series A, Containing Papers of a Mathematical and Physical Character*, 136(830):619–630, 1932.

[9] John Cockcroft and Ernest Walton. Experiments with high velocity positive ions. ii. -the disintegration of elements by high velocity protons. *Proceedings of the Royal Society of London. Series A, Containing Papers of a Mathematical and Physical Character*, 137(831):229–242, Jul 1932.

[10] Robert Jemison Van de Graaff. A 1500000 volt electrostatic generator. *Physical Review Journals*, 38, 1931.

[11] R. J. Van de Graaff, K. T. Compton, and L. C. Van Atta. The electrostatic production of high voltage for nuclear investigations. *Phys. Rev.*, 43:149–157, Feb 1933.

[12] G. Ising. *Prinzip einer Methode zur Herstellung von Kanalstrahlen hoher Voltzahl*. Arkiv för Matematik, Astronomi och Fysik. Almqvist & Wiksells Boktryckeri-A.B., 1924.

[13] Rolf Wideröe. Über ein neues prinzip zur herstellung hoher spannungen. *Archiv für Elektrotechnik*, 21(4):387–406, 1928.

[14] Ernest O. Lawrence and M. Stanley Livingston. The production of high speed light ions without the use of high voltages. *Phys. Rev.*, 40:19–35, Apr 1932.

[15] Vladimir Veksler. A new method of accelerating relativistic particles. *Proceedings of the USSR Academy of Sciences*, 43(8):346–348.

[16] Cern accelerating science. `https://home.cern/science/accelerators/large-hadron-collider`.

[17] R. Wideröe. Some memories and dreams from the childhood of particle accelerators. *Europhysics News*, 15(2):9–11, 1984.

[18] D. W. Kerst, G. D. Adams, H. W. Koch, and C. S. Robinson. Operation of a 300-mev betatron. *Phys. Rev.*, 78:297–297, May 1950.

[19] T. Tajima and J. M. Dawson. Laser electron accelerator. *Phys. Rev. Lett.*, 43:267–270, Jul 1979.

[20] A. J. Gonsalves, K. Nakamura, J. Daniels, C. Benedetti, C. Pieronek, T. C. H. de Raadt, S. Steinke, J. H. Bin, S. S. Bulanov, J. van Tilborg, C. G. R. Geddes, C. B. Schroeder, Cs. Tóth, E. Esarey, K. Swanson, L. Fan-Chiang, G. Bagdasarov, N. Bobrova, V. Gasilov, G. Korn, P. Sasorov, and W. P. Leemans. Petawatt laser guiding and electron beam acceleration to 8 gev in a laser-heated capillary discharge waveguide. *Phys. Rev. Lett.*, 122:084801, Feb 2019.

[21] Doebert. Gradient limitations for high-frequency accelerators. Sep 2004.

[22] V. Malka. Electron acceleration by a wake field forced by an intense ultrashort laser pulse. *Science*, 298(5598):1596–1600, 2002.

[23] E. Esarey, C. B. Schroeder, and W. P. Leemans. Physics of laser-driven plasma-based electron accelerators. *Rev. Mod. Phys.*, 81:1229–1285, Aug 2009.

[24] L. V. Keldysh. Ionization in the field of a strong electromagnetic wave. *Journal of Experimental and Theoretical Physics*, 20(5):1307–1314, May 1965.

[25] A. M. Zheltikov. Keldysh parameter, photoionization adiabaticity, and the tunneling time. *Phys. Rev. A*, 94:043412, Oct 2016.

[26] Atomic data for helium (he). `https://physics.nist.gov/PhysRefData/Handbook/Tables/heliumtable1.htm`.

[27] BW Boreham and JL Huges. Measurement of ionization threshold intensities in helium using ponderomotive force accelerated electrons. *Sov. Phys. JETP*, 53:252–259, 1981.

[28] K. Wiesemann. A short introduction to plasma physics. *CAS-CERN Accelerator School: Ion Sources - Proceedings*, 04 2014.

[29] M. C. Downer, R. Zgadzaj, A. Debus, U. Schramm, and M. C. Kaluza. Diagnostics for plasma-based electron accelerators. *Rev. Mod. Phys.*, 90:035002, Aug 2018.

[30] D.A. Bromley Walter Greiner. *Classical Electrodynamics*. Classical theoretical physics. Springer, 1 edition, 1998.

[31] Guillaume Genoud. *Laser-Driven Plasma Waves for Particle Acceleration and X-ray Production*. PhD thesis, 2011.

[32] S. Bulanov, N. Naumova, F. Pegoraro, and J. Sakai. Particle injection into the wave acceleration phase due to nonlinear wake wave breaking. *Phys. Rev. E*, 58:R5257–R5260, Nov 1998.

[33] C. Rechatin, J. Faure, A. Ben-Ismail, J. Lim, R. Fitour, A. Specka, H. Videau, A. Tafzi, F. Burgy, and V. Malka. Controlling the phase-space volume of injected electrons in a laser-plasma accelerator. *Phys. Rev. Lett.*, 102:164801, Apr 2009.

[34] K. Schmid, A. Buck, C. M. S. Sears, J. M. Mikhailova, R. Tautz, D. Herrmann, M. Geissler, F. Krausz, and L. Veisz. Density-transition based electron injector for laser driven wakefield accelerators. *Phys. Rev. ST Accel. Beams*, 13:091301, Sep 2010.

[35] A. Pak, K. A. Marsh, S. F. Martins, W. Lu, W. B. Mori, and C. Joshi. Injection and trapping of tunnel-ionized electrons into laser-produced wakes. *Phys. Rev. Lett.*, 104:025003, Jan 2010.

[36] C. McGuffey, A. G. R. Thomas, W. Schumaker, T. Matsuoka, V. Chvykov, F. J. Dollar, G. Kalintchenko, V. Yanovsky, A. Maksimchuk, K. Krushelnick, V. Yu. Bychenkov, I. V. Glazyrin, and A. V. Karpeev. Ionization induced trapping in a laser wakefield accelerator. *Phys. Rev. Lett.*, 104:025004, Jan 2010.

[37] M. Mirzaie, S. Li, M. Zeng, N. A. M. Hafz, M. Chen, G. Y. Li, Q. J. Zhu, H. Liao, T. Sokollik, F. Liu, and et al. Demonstration of self-truncated ionization injection for gev electron beams. *Scientific Reports*, 5(1), 2015.

[38] W. Lu, M. Tzoufras, C. Joshi, F. S. Tsung, W. B. Mori, J. Vieira, R. A. Fonseca, and L. O. Silva. Generating multi-gev electron bunches using single stage laser wakefield acceleration in a 3d nonlinear regime. *Phys. Rev. ST Accel. Beams*, 10:061301, Jun 2007.

[39] V. Ginzburg and I. Frank. To the theory of transition radiation. *Sov. Phys. JETP*, 16, 1946.

[40] C. B. Schroeder, E. Esarey, J. van Tilborg, and W. P. Leemans. Theory of coherent transition radiation generated at a plasma-vacuum interface. *Phys. Rev. E*, 69:016501, Jan 2004.

[41] Boris M Bolotovskii and Alexander V Serov. Features of the transition radiation field. *Physics-Uspekhi*, 52(5):487–493, 2009.

[42] M. Villavicencio and J. L. Jiménez. Boundary conditions and generalized functions in a transition radiation problem. *The European Physical Journal Plus*, 132(3), 2017.

[43] V.a Verzilov. Transition radiation in the pre-wave zone. *Physics Letters A*, 273(1-2):135–140, 2000.

[44] Boris Dolgoshein. Transition radiation detectors. *Nuclear Instruments and Methods in Physics Research Section A: Accelerators, Spectrometers, Detectors and Associated Equipment*, 326(3):434–469, 1993.

[45] Julien Bergoz and Bergoz. Current monitors for particle beams. *Nuclear Physics A*, 525:595–600, 1991.

[46] Biezl. Stromwandler zeichnung. `https://commons.wikimedia.org/wiki/File:Stromwandler_Zeichnung.svg`, 2009.

[47] B. Hidding, G. Pretzler, M. Clever, F. Brandl, F. Zamponi, A. Lübcke, T. Kämpfer, I. Uschmann, E. Förster, U. Schramm, and et al. Novel method for characterizing relativistic electron beams in a harsh laser-plasma environment. *Review of Scientific Instruments*, 78(8):083301, 2007.

[48] Y. Glinec, J. Faure, A. Guemnie-Tafo, V. Malka, H. Monard, J. P. Larbre, V. De Waele, J. L. Marignier, and M. Mostafavi. Absolute calibration for a broad range single shot electron spectrometer. *Review of Scientific Instruments*, 77(10):103301, 2006.

[49] John Burkardt and Catalin Trenchea. Refactorization of the midpoint rule. *Applied Mathematics Letters*, 107:106438, 2020.

[50] X.L. Xu, C.-H. Pai, C.J. Zhang, F. Li, Y. Wan, Y.P. Wu, J.F. Hua, W. Lu, W. An, P. Yu, and et al. Nanoscale electron bunching in laser-triggered ionization injection in plasma accelerators. *Physical Review Letters*, 117(3), 2016.

[51] J. R. Fienup. Phase retrieval algorithms: a comparison. *Appl. Opt.*, 21(15):2758–2769, Aug 1982.

[52] M. Heigoldt, A. Popp, K. Khrennikov, J. Wenz, S. W. Chou, S. Karsch, S. I. Bajlekov, S. M. Hooker, and B. Schmidt. Temporal evolution of longitudinal bunch profile in a laser wakefield accelerator. *Phys. Rev. ST Accel. Beams*, 18:121302, Dec 2015.

[53] Eli beamlines facility division. `https://www.fzu.cz/en/research/divisions-and-departments/division-9`.

[54] Turbo-ict bcm-rf-e - ultra short bunch and very low charge measurement. `https://www.bergoz.com/products/turbo-ict/`, Apr 2021.

[55] Minion Interactive s.r.o. Yag:ce. `https://www.crytur.cz/materials/yagce/`.

[56] Yag(ce) - yttrium aluminium garnate (cesium). https://www.advatech-uk.co.uk/yag_ce.html.

[57] Cassettes and screens: Radiology: Film solutions: Carestream health, inc.

[58] Davy Gérard and Stephen K. Gray. Aluminium plasmonics. *Journal of Physics D: Applied Physics*, 48(18):184001, 2014.

[59] S. I. Bajlekov, M. Heigoldt, A. Popp, J. Wenz, K. Khrennikov, S. Karsch, and S. M. Hooker. Longitudinal electron bunch profile reconstruction by performing phase retrieval on coherent transition radiation spectra. *Physical Review Special Topics - Accelerators and Beams*, 16(4), 2013.

[60] Gallium arsenide: lenses, windows, mirrors, filters and prisms. https://www.globalopticsuk.com/gaas/, Feb 2021.

[61] Flame vis-nir spectrometers. https://www.oceaninsight.com/products/spectrometers/general-purpose-spectrometer/flame-series/flame-vis-nir/.

[62] Flame-nir spectrometer. https://www.oceaninsight.com/products/spectrometers/general-purpose-spectrometer/flame-series/FLAME-NIR/.

[63] Zinc selenide window lens - znse: mirrors, filters and prisms. https://www.globalopticsuk.com/zinc-selenide/, Feb 2021.

[64] 2dmct mid-ir detector for ultrafast spectroscopy. http://phasetechspectroscopy.com/products/2dmct/.

List of Figures

1 New Zealand post stamp portraying Ernest Rutherford. Reproduced from https://www.sciencedirect.com 2
2 First Cockcroft-Walton Accelerator. Retrieved from [8] 3
3 Schematic view of the large generator. Retrieved from [11] 4
4 The diagram of a cyclotron. Retrieved from [14] 4
5 The scale of Large Hadron Collider. Reproduced from *Symmetry Magazine* 5

1.1 Tunneling of the electron through the potential of the atomic nucleus. Reproduced from [25] 9
1.2 Numerical solutions to the equation (1.21) for right-propagating lasers. The green area depicts the laser pulse, the blue line are the density oscillations(equation 1.22), the red line shows the accelerating fields. 13
1.3 Calculated maximum density oscillations created by laser pulses with different lengths. In all cases, normalized vector potential amplitude was $a_0 = 1$. 14

2.1 Electric field of charge (a) instantaneously starting, (b) instantaneously stopping. Reproduced from [41] 17
2.2 Far-field intensity profile of 100 MeV electron given by the equation (2.1) 18

3.1 Schematics of the ICT. Reproduced from [46] 22
3.2 Trajectories of electrons with different energies passing through the magnetic field (blue rectangle) and hitting the image plane (red line) 23
3.3 Electrons with two different energies and angles 24
3.4 Mono-energetic bunch with 3 different electrons 25
3.5 UI of the Magnetic Spectrometer App for an arbitrary custom experimental setup and electron bunch with zero pointing 26
3.6 *Left*: The *Magnet Parameters* window for magnetic field settings. *Right*: The *Scintillator* window for image plane settings 27
3.7 The *Electron Bunch Angular Distribution* window 27
3.8 *Scintillator Results* for the arbitrary setup shown in Figure 3.5. a) Detections observed on the scintillating screen colored according to their energy shown on the colorbar on the right. b) Dependence of zero pointing electron energy on the horizontal position on the scintillator 28
3.9 Transition radiation spectra for Gaussian beams with different σ_z. a) Beam profiles, b) Corresponding spectra 29
3.10 Effect of internal substructures on Transition Radiation. a) Longitudinal distribution, b) Corresponding transition radiation spectra 30

4.1 Laser L3 HALPS. Reproduced from [53] 32
4.2 Illustration of laser wakefield electron acceleration at ELI-Beamlines 32
4.3 Integrating Current Transformer *The Turbo-ICT-VAC-055*. Reproduced from [54] 33

4.4 Magnetic Spectrometer Illustration 34
4.5 Dipole magnetic spectrometer with the peak magnetic field of up to 1 T 34
4.6 Cross-section of the measured magnetic field of the magnet with resolution 2mm 35
4.7 Comparison of the calculations with homogeneous 1T magnetic field and the real magnetic field. a) Homogeneous 1T magnetic field, b) Real magnetic field 35
4.8 Numerical Calibration of the Magnetic Spectrometer 36
4.9 Emissivity analysis of the image plane devices. a) YAG:Ce scintillator made by CRYTUR. b) YAG:Ce scintillator made by Advatech UK c) Lanex scintillator made by Carestream 37
4.10 Experimental design of the Transition Radiation Detector setup . 39

A. Appendix

A.1 Ponderomotive force

In the equation 1.2 in the chapter 1.1 we derived the ponderomotive force affecting the charged particle in the presence of an oscillating electromagnetic field, where we used the identity $\boldsymbol{A} \times (\nabla \times \boldsymbol{A}) = \frac{1}{2}\nabla|\boldsymbol{A}|^2 - (\boldsymbol{A} \cdot \nabla)\boldsymbol{A}$. In this identity, $(\boldsymbol{A} \cdot \nabla)\boldsymbol{A}$ is identically zero. This can be shown by considering the fact, that the vector potential is transversal and depends only on the time and z-axis, i.e. $\boldsymbol{A} = (A_x(z,t), A_y(z,t), 0)$. Calculating the dot product therefore results in

$$\boldsymbol{A} \cdot \nabla = (A_x(z,t), A_y(z,t), 0) \cdot (\partial/\partial x\ ,\ \partial/\partial y\ ,\ \partial/\partial z\,) = A_x(z,t)\frac{\partial}{\partial x} + A_y(z,t)\frac{\partial}{\partial y}\,.$$

Multiplying this result by $\boldsymbol{A}$ then yields

$$\left(A_x(z,t)\frac{\partial A_x(z,t)}{\partial x} + A_y(z,t)\frac{\partial A_x(z,t)}{\partial y}, A_x(z,t)\frac{\partial A_y(z,t)}{\partial x} + A_y(z,t)\frac{\partial A_y(z,t)}{\partial y}, 0\right)$$

Since both A_x and A_y depend only on z and t, the previous expression is identically zero.

A.2 MidPoint method in Magnetic Spectrometer App

Code for the MidPoint method used in the Magnetic Spectrometer App. Code of the whole app is much longer, this is only the part of it.

```
gamma = zeros(1,length(t)-1); %preallocating Lorentz
    factor array

%initializing initial conditions for current simulation
% each column represents one point in time
% each row represents one coordinate (x,y,z)
r = [-app.L_x/2-app.source_distance;0;0]; %initial
    position
p = [sqrt(1-sin(app.divergence_data(1,i_div))^2-sin(app.
    divergence_data(2,i_div))^2);-sin(app.divergence_data
    (1,i_div));sin(app.divergence_data(2,i_div))]*i_gamma*
    app.m*app.c; %initial momentum

%====calculating trajectory for specific initial gamma====
dt = 100*(app.Scintillator_Radius+app.source_distance)/(
    app.c*10^5*app.SimulationprecisionSpinner.Value); %time
     step
t = (0:dt:100000*dt*app.SimulationprecisionSpinner.Value);
     %total time

%=====calculating the trajectory=====
for i=1:(length(t)-1)
    gamma(i) = sqrt(1+(norm(p(:,i))/app.m/app.c)^2); %
        calculating Lorentz factor
    if (-app.L_x/2< r(1,i)) && ( r(1,i) < app.L_x/2 ) &&
       (-app.L_y/2< r(2,i)) && (r(2,i) < app.L_y/2) && (-
       app.L_z/2< r(3,i)) && (r(3,i) < app.L_z/2) %
       checking if electron is in magnetic field
        if app.magnetic_field_switch == "1" %checking in
           which state the switch was, in this case the
           homogenous magnetic field was chosen, option
           "1"
            B_used = app.B; %app.B is the magnetic field
               from the window with magnetic field, B_used
                is going to be used for calculations few
               lines later
        elseif app.magnetic_field_switch == "2"
            F = [abs(app.magnetic_field_data(:,1)-r(1,i))+
               abs(app.magnetic_field_data(:,2)-r(2,i))+
               abs(app.magnetic_field_data(:,3)-r(3,i))
               app.magnetic_field_data(:,4)]; %calculating
                distances of the electron from all points
```

```
            with data using manhattan metric
        F = sortrows(F,1); %sorting by the sum off all
            distances
        B_used = mean(F(1:4,2)); %using the mean value
            of magnetic field from 4 nearest
           neighbours
        disp(B_used);
    end

%====MidPoint Method====
    p_dt_2 = p(:,i) + app.e*(cross(p(:,i),[0;0;-B_used
        ])/app.m/gamma(i))*dt/2;
    p(:,i+1) = p(:,i) + app.e*(cross(p_dt_2,[0;0;-
        B_used])/app.m/gamma(i))*dt;
else %if electron is not in the magnetic field, then
   momentum does not change
    p_dt_2 = p(:,i);
    p(:,i+1)=p(:,i);
end

r(:,i+1)=p_dt_2/app.m/gamma(i)*dt+r(:,i); % change in
   coordinates
```